



Relativistic and Spin-Orbit Dynamics at Non-Relativistic Intensities in Strong-Field Ionization

Andrew S. Maxwell ^{1,*} and Lars Bojer Madsen ¹

¹*Department of Physics and Astronomy, Aarhus University, DK-8000 Aarhus C, Denmark*

(Dated: August 30, 2023)

Spin-orbit dynamics and relativistic corrections to the kinetic energy in strong-field dynamics, have long been ignored for near- and mid-IR fields with intensities 10^{13} – 10^{14} W/cm², as the final photoelectron energies are considered too low for these effects to play a role. However, using a precise and flexible path-integral formalism, we include all correction terms from the fine-structure, Breit-Pauli Hamiltonian. This enables a treatment of spin, through coherent spin-states, which is the first model to use this approach in strong-field physics. We are able to show that the most energetically rescattered wavepackets, undergo huge momentum transfer and briefly reach relativistic velocities, which warrants relativistic kinetic energy corrections. We probe these effects and show that they yield notable differences for a 1600 nm wavelength laser field on the dynamics and the photoelectron spectra. Furthermore, we find that the dynamical spin-orbit coupling is strongly overestimated if relativistic corrections to kinetic energy are not considered. Finally, we derive a new condition that demonstrates that relativistic effects begin to play a role at intensities orders of magnitude lower than expected. Our findings may have important implication for imaging processes such as laser-induced electron diffraction, which includes high-energy photoelectron recollisions.

I. INTRODUCTION

Electron spin is a canonical example of the departure of the atomic scale world from our macroscopic one. The discovery of spin [1] carried huge fundamental significance, while also leading to a vast range of observable effects, from fine structure splitting and the Zeeman [2] effect, to the Stern-Gerlach experiment and Mott scattering [3]. There are a huge range of applications exploiting spin, including spin resonance imaging processes, atomic clocks, quantum sensors for magnetic fields, spin qubits, and spintronics (spin transport in solids) [3]. Despite its significance, until recently [4, 5], the role of spin was ignored in strong-field processes driven by “non-relativistic” laser intensities. The argument given is that at these intensities, the spin will not interact with the laser field, and that the energies reached in laser driven recollisions (often taken to be $\approx 3.17U_p$ [6], U_p is the ponderomotive energy, i.e., the cycle-averaged kinetic energy of a free electron in the laser field) are insufficient for spin-orbit coupling or other relativistic effects to play a role.

Strong-field physics deals with the interaction of intense and short laser fields with matter. Through the control of a few recollision-based processes, this has enabled the measurement and manipulation of matter on the scale of attoseconds (10^{-18} s), giving birth to the field of attosecond physics [7–10] and attosecond laser pulses [11, 12] via high-harmonic generation (HHG) [6, 13]. One of the primary processes involved is above-threshold ionization (ATI) [14], which, in this context, is the strong-field (or tunnel) removal of an electron by the laser. After ionization, the continuum electron may undergo laser

driven elastic scattering off the residual ion, sometimes referred to as high-order ATI (HATI) [15, 16]. The processes of ATI and HATI have found use in imaging procedures, laser-induced electron diffraction (LIED) [17–21] and photoelectron holography [22–24]. In the former, the recolliding electron is used to provide diffraction images of its parent molecule. In photoelectron holography, the interference of electronic wavepackets that recollide and those that do not, is used to image the parent atom or molecule. In the case of LIED, long wavelengths, on the order of a few microns, are used to achieve high electronic recollision velocities. These hard recollisions closely probe the target, potentially leading to large spin-orbit coupling and large kinetic energies.

In the relativistic laser intensity regime ($I > 10^{16}$ W/cm²), see e.g., Refs. [25–34], spin is considered by necessity, note we have neglected works on high intensity and high frequency (in the so-called stabilization regime), as we are focused on fields with near-infrared and infrared frequencies. Popular ionization models such as the strong-field approximation (SFA) [35–37] were generalized to the relativistic regime [25, 26], and many studies have considered spin related effects, see e.g., Refs. [28, 31]. However, in order to estimate the intensity at which relativistic effects become relevant, it is common to employ classical Coulomb-free trajectories [27], which predicts that these effects should be negligible for intensities $I < 10^{16}$ W/cm². This is a good approach for the direct ATI electrons, but in the case of rescattered electrons, the Coulomb potential can allow for much higher kinetic energies to be reached. In this work, we will introduce a Coulomb adapted condition for backscattered trajectories. Some relativistic models have extended the relativistic SFA to account for the Coulomb potential, see e.g., Refs. [33, 34], and derived cutoff limits for relativistic rescattering [32].

In the non-relativistic regime, the effect of spin and

* andrew.maxwell@phys.au.dk

spin-orbit coupling was found to play a role in atoms with appreciable internal spin-orbit coupling. Early work demonstrated spin-orbit effects in ion alignment with strong laser fields [38]. Spin-orbit effects in particular cases in single- [39] and multi- [40] photon ionization have long been known, but in Ref. [4], this was theoretically described for strong-field ionization with a circularly polarized laser field (later extended to a two colour field [41]), where a general mechanism for producing spin polarized electrons was developed. This mechanism depends on the preferential tunnelling of ‘counter’-rotating electrons to the circular laser field [42–44]. The spin polarized electrons were experimentally verified by Ref. [5], where Mott scattering was used to measure the spin polarization of the photoelectrons. Later experiments revealed different spin-polarization across peaks in the photoelectron ATI spectra [45]. Subsequent theoretical work has focused on effects due to Pauli symmetrization given initial singlet or triplet states [46, 47], or the spin dynamics of the residual ion [48–50], related work using attosecond pulses has demonstrated the possibility to reveal time-resolved spin dynamics in the ion [51]. In a very recent work [52], inelastic recollision of the photoelectron with the ion was also considered, where tuning the evolution of the ionic spin could allow a spin flip, which has implications for recollision based imaging process such as LIED.

Thus, the potential for spin and spin-orbit coupling to play a role in the photoelectron recollision processes has only just begun to be explored. In this work, we will explore the spin and spin-orbit coupling of the recolliding photoelectron in detail. In order to do this, we will extend the accurate and flexible path-integral approach, the Coulomb quantum-orbit strong-field approximation (CQSFA) [53–58]. This model has been developed in the spirit of the quantum-orbit formalisms of the SFA [59–61], that has enabled significant insight into ATI and recollision processes [15, 16]. In its original formulation, the CQSFA was used extensively to understand holographic interference patterns that occur in photoelectron momentum distributions (PMDs) [62–65]. In these studies, a good qualitative agreement with numerical solutions of the time-dependent Schrödinger equation (TDSE) was possible for medium photoelectron energies of up to around $3\text{--}4U_p$. However, recent developments [66–68] have enabled exceptional quantitative agreement with the TDSE up to the highest rescattering energies of $10U_p$. These developments include, the proper computation of the stability prefactor and Maslov phases [66], an improved algorithm for finding saddle-point solutions, the inclusion of a \sin^2 pulse envelope, and an improved method for computing the bound-state prefactors, all these improvements are combined in Ref. [68], and have been used in this work.

The CQSFA provides the ideal platform for understanding the spin-orbit effects of the recolliding photoelectron, providing an intuitive trajectory-based picture. In this work, we demonstrate the high level of agreement

of the CQSFA for the non-relativistic spin-less, few-cycle case, via comparison with a TDSE solver at a wavelength of 1600 nm for hydrogen at a typical intensity of 5×10^{13} W/cm². We demonstrate, even at this stage, that relativistic corrections are required to correctly describe the rescattered wavepacket, due to trajectories that reach superluminal velocities. Thus, we present a derivation for the CQSFA that includes the Breit-Pauli relativistic corrections, in particular, a spin-orbit coupling term and corrections to the kinetic energy (or mass correction term). Inclusion of coherent-spin states, allows for a dynamical description of spin with path integrals. We derive analytic expressions that describe the spin dynamics and evolution of the spin-orbit phase. We find that with the kinetic energy corrections, the rescattering dynamics is properly described, with trajectories no longer travelling faster than light. This leads to a noticeable change in the PMD probability that can be explained in terms of the trajectories. Furthermore, we consider the effect of initial spin-alignment vs no spin-alignment. If the relativistic kinetic energy corrections are not included, this leads to considerable differences that would be experimentally measurable. However, including the kinetic energy corrections, leads to very modest differences for the two spin alignments. This demonstrates the importance of including the relativistic kinetic energy corrections when computing the effect of spin-orbit coupling. Finally, we derive analytical expressions to approximately identify the (back)-scattering angles for which a relativistic treatment is required across a range of laser intensities.

The article is organized as follows. In Sec. II we briefly describe the theory for the non-relativistic spin-less CQSFA and TDSE solver. In Sec. III, we present the results of these models and investigate the rescattered trajectories. In Sec. IV, we present the new formulation of the CQSFA, including spin and other relativistic corrections. In Sec. V, analytical results are presented regarding the weak-coupling approximation and spin-orbit phase. In Sec. VI, we present the results with the newly derived theory, investigating the effect of the relativistic kinetic energy corrections and spin-orbit coupling terms. In Sec. VII, we derive limits to determine at which scattering angles a relativistic treatment is required. Finally, in Sec. VIII, we present our final conclusions. Atomic units are used throughout unless stated otherwise.

II. THEORY

A. CQSFA

We begin by giving a brief description of the CQSFA, which has been described in detail in its present accurate form in Ref. [68], while its initial development is described in Refs. [53, 55, 56].

We start from the non-relativistic Hamiltonian for an atomic target in a strong-field under the single-active-

electron approximation, which may be written as

$$\hat{H}(t) = \hat{H}_0 + \hat{H}_I(t). \quad (1)$$

Here, \hat{H}_0 is the Hamiltonian atomic system, which, we write as $\hat{H}_0 = K(\hat{\mathbf{p}}) + U(\hat{\mathbf{r}})$, where $K(\hat{\mathbf{p}})$ and $U(\hat{\mathbf{r}})$ are general functions for the kinetic and potential energies, respectively, while $\hat{H}_I(t) = \hat{\mathbf{r}} \cdot \mathbf{E}(t)$ describes the interaction with the external laser field in the length gauge. We want to compute the momentum-dependent transition amplitude $M(\mathbf{p}) = \langle \psi_{\mathbf{p}} | U(t, t_0) | \psi_0 \rangle$, where $|\psi_0\rangle$ is the initial bound state of the system, $|\psi_{\mathbf{p}}\rangle$ is a scattering state with asymptotic momentum \mathbf{p} , the final time $t \rightarrow \infty$, and the initial time $t_0 \rightarrow -\infty$. The transition amplitude may be written, still in an exact form, [53, 55] as

$$M(\mathbf{p}) = -i \int_{-\infty}^t dt' \langle \psi_{\mathbf{p}} | U(t, t') H_I(t') | \psi_0(t') \rangle, \quad (2)$$

while insertion of the resolution of the identity operator before $H_I(t')$, given by $\mathbb{1}_3 = \int d^3\mathbf{p}_0 |\tilde{\mathbf{p}}_0\rangle \langle \tilde{\mathbf{p}}_0|$, where $\tilde{\mathbf{p}}_0 = \mathbf{p}_0 + \mathbf{A}(t')$, enables representation in path-integral form

$$M(\mathbf{p}) = -i \int_{-\infty}^{\infty} dt' \int_{\mathbf{r}(t')} \frac{\mathcal{D}'\mathbf{r}}{(2\pi)^3} \int^{\mathbf{p}(t)} \mathcal{D}'\mathbf{p} e^{iS[\mathbf{r}, \mathbf{p}, t']} d(\tilde{\mathbf{p}}_0, t'), \quad (3)$$

with $d(\tilde{\mathbf{p}}_0, t') = \langle \mathbf{p}_0 + \mathbf{A}(t') | H_I(t') | \psi_0 \rangle$,

$S[\mathbf{r}, \mathbf{p}, t'] =$

$$I_{\mathbf{p}} t' - \mathbf{p}(t') \cdot \mathbf{r}(t') - \frac{1}{2} \int_{t'}^{\infty} d\tau (\dot{\mathbf{p}} \cdot \mathbf{r} + H[\mathbf{r}, \mathbf{p}, t']), \quad (4)$$

and $H[\mathbf{r}, \mathbf{p}, t']$ is the classical Hamiltonian [69]. The action in Eq. (4) results from enforcing an initial condition in position-space and a final limit in momentum space, giving rise to the boundary term $\mathbf{p}(t') \cdot \mathbf{r}(t')$, i.e., we are in the mixed representation. These restrictions are denoted by the primes on \mathcal{D} 's, full details are given in Ref. [68]. For atoms, the initial position is the origin, hence $\mathbf{r}(t') = \mathbf{0}$, and $\mathbf{p}(t') \cdot \mathbf{r}(t')$ may be dropped. Note, we define $\mathbf{p}_0 = \mathbf{p}(t') = \mathbf{p}(\text{Re}[t'])$, which results from taking momentum fixed during tunnelling, this approximation is explained in more detail in Appendix A.

The transition amplitude of Eq. (3) is then evaluated via the saddle-point approximation

$$M(\mathbf{p}) = -i \sum_s \sqrt{\frac{2\pi i}{\partial^2 S / \partial t'^2}} \frac{e^{-i\pi\nu/2}}{\sqrt{|J|}} d(\tilde{\mathbf{p}}_{0s}, t_s) e^{iS[\mathbf{r}_s, \mathbf{p}_s, t_s]}, \quad (5)$$

where $\underline{J} = \frac{\partial \mathbf{p}_f}{\partial \mathbf{p}_0}$, $J = \det(\underline{J})$, and ν is the Maslov phase, which may be determined by computing \underline{J} at all points in time and counting the number of focal points ($J = 0$)

Orbit	Π_z	Π_{\perp}	Behaviour
1	+	+	Direct
2	-	+	Laser-driven deflection
3	-	-	Forward Scattered
4	+	-	Rescattered

TABLE I. Orbit classification used in the CQSFA for monochromatic linearly polarized fields. The labelling 1 to 4 classifies the orbit with two different conditions, the signs of $\Pi_z = z_0 p_{fz}$ and $\Pi_{\perp} = p_{fx} p_{0x} + p_{fy} p_{0y}$, respectively. The behaviour in the fourth column indicates the expected dynamics of the specific types of orbits.

[66, 68]. The sum runs over solutions to the saddle-point equations, which are given by

$$(\mathbf{p}_{0s} + \mathbf{A}(t_s))^2 + 2I_{\mathbf{p}} = 0 \quad (6)$$

$$\dot{\mathbf{r}}_s(t) = \nabla_{\mathbf{p}} K[\mathbf{p}_s] \quad \dot{\mathbf{p}}_s(t) = -\nabla_{\mathbf{r}} U[\mathbf{r}_s]. \quad (7)$$

Equation (6) leads to complex ionization times t_s meaning the integral in Eq. (4) is done in two parts, first over imaginary time from t_s to $\text{Re}[t_s]$ associated with tunnelling, then over real time from $\text{Re}[t_s]$ to ∞ , associated with real-space continuum propagation, see Appendix A for more details.

The CQSFA solves a boundary value problem known as the inverse problem, i.e., all solutions of Eqs. (6) and (7) (a.k.a. trajectories or quantum orbits) are found satisfying $\mathbf{r}(t') = \mathbf{0}$ and $\mathbf{p}(t \rightarrow \infty) = \mathbf{p}_f$. There will be multiple solutions for each final momentum point, each solution can be uniquely determined by its initial momentum coordinate \mathbf{p}_0 . Thus, the inverse problem reduces to finding the set of initial momentum coordinates \mathbf{p}_0 , for each final momentum \mathbf{p}_f .

The approach just described is different from the majority of models, which use a forward approach and bin trajectories with similar final momenta, which requires small bins and many trajectories to resolve interferences, while the inverse approach allows for many fewer trajectories. Furthermore, recent work [70] has identified that forward approaches do not yield the correct sampling weight in terms of the Jacobian J , leading to $1/|J|$ instead of the correct $1/\sqrt{|J|}$ computed by inverse approaches. The downside of the inverse approach is that it is much harder to solve, and approaches can be less general. In previous works [55–57], solutions were found by ‘exploring’ the manifold of solutions, i.e., changing parameters to find ‘connected’ solutions. This method is very fast but has two disadvantages; (i) it requires pre-knowledge of the shape of the manifold and, where solutions lie, which changes from system to system; (ii) it assumes all solutions can be reached in this way, which is not the case. In this work, we used an alternative method [68] where the solutions are found by initial random sampling of \mathbf{p}_0 , and adaptively concentrating guesses in \mathbf{p}_0 regions where dense clusters of solutions are found. This method is more general and allows all solutions to be found regardless of the system.

The distinct solutions for each \mathbf{p}_f do not have an exhaustive classification, however, in the case of linearly polarized fields, four broad types of orbit can be defined that can helpfully classify behaviour. This classification uses the tunnel exit

$$z_0 = \text{Re} \left[\int_{t_s}^{\text{Re}[t_s]} d\tau A_z(\tau) \right], \quad (8)$$

and initial momentum perpendicular to the laser polarization $\mathbf{p}_{0\perp}$, and compares their sign with p_{fz} and $\mathbf{p}_{f\perp}$, respectively. Then we may define $\Pi_z = z_0 p_{fz}$ and $\Pi_\perp = p_{fx} p_{0x} + p_{fy} p_{0y}$. This is the same definition as in Ref. [68], which generalizes the commonly employed 2D classification [55, 67, 71] to 3D. The classification, summarized in Table I, is as follows; $\Pi_z > 0 \wedge \Pi_\perp > 0$: orbit 1, associated with direct trajectories that do not return to the parent atom; $\Pi_z < 0 \wedge \Pi_\perp > 0$: orbit 2, describes trajectories that undergo a laser driven return but do not interact strongly with the parent atom; $\Pi_z < 0 \wedge \Pi_\perp < 0$: orbit 3, trajectories that forward scatter off the parent atom; and $\Pi_z < 0 \wedge \Pi_\perp < 0$: orbit 4, associated with trajectories that back-scatter off parent atom. Note, that there may be more than one valid solution of each type.

Examples typifying the classifications are given in FIG. 1(a); laser parameters are given in the caption. Here we see typical examples of orbits 1-4, as well as an ‘atypical’ orbit 4 (labelled 4b), along with the corresponding ionization times in the panel below. For this study, we are most interested in the rescattered trajectories of orbit 4. The tunnel exit of the ‘typical’ orbit 4 lies at $z_0 \approx -15$ a.u., from here the laser drives the trajectory away and then back again, undergoing a laser driven return, as shown in FIG. 1(a). Thus, this solution belongs to a well-studied category of returning trajectory known from HHG and ATI [13, 15]. These orbits come in pairs, long and short. Here, we have only plotted the long trajectory as the short’s path would be very similar. These pairs can be seen in FIG. 1(b) in every half cycle by black loops extending in opposite directions each half cycle. The solution pairs form loops because at a classical boundary, they coalesce, forming the rescattering ridge in the PMD, see FIG. 2. In contrast, the directly recolliding orbit 4b has a tunnel exit of $z_0 \approx -20$ a.u. close to orbit 1’s tunnel exit. Instead of undergoing a laser driven recollision the initial conditions are such that the trajectory returns before the laser has considerably changed sign. These trajectories also occur every half cycle and are connected to the ‘typical’ recolliding orbits via orbit 3 on a continuous manifold. Orbit 4b ionizes far from the peak at near zero field, thus the probability of these orbits is very low, however, they undergo a very strong recollision, so provide an interesting case to study. If the probability of these trajectories could be increased, they could be used for very strongly probing targets.

B. TDSE

To benchmark the CQSFA results, we solve the TDSE using the freely available QPROP [72] software. QPROP is a single-active-electron TDSE solver, which implements a fast and accurate method for the calculation of PMD using the i-SURFF projection method. To model hydrogen, a Coulomb potential is employed. In this computation, we considered angular momenta up to $l = 200$, grid spacing $\Delta r = 0.1$ a.u., and time step $\Delta t = 0.05$ a.u, and we checked the results for convergence.

In both the CQSFA and QPROP we consider a \sin^2 laser field, where the vector potential is defined by

$$\mathbf{A}(t) = 2\sqrt{U_p} \sin^2 \left(\frac{\omega t}{2N} \right) \cos(\omega t + \phi), \quad (9)$$

with N being the number of laser cycles of the vector potential envelope, while U_p is the ponderomotive energy or quiver energy of the free electron in the laser field, which is proportional to the peak laser intensity $I_0 = 2U_p c \epsilon_0 \omega^2$. The angular frequency is given by ω and the carrier envelope phase (CEP) is given by ϕ . We focus on a wavelength $\lambda = 1600$ nm, i.e., $\omega = 0.0285$ a.u.

III. NON-RELATIVISTIC RESULTS

In FIG. 2, we show a validation of the CQSFA vs the non-relativistic-TDSE with PMDs for hydrogen at a wavelength of 1600 nm for a 4-cycle and 6-cycle \sin^2 pulse, panels (a) and (b), respectively. Very good agreement is seen between the two models across the whole momentum region. There is some deviation across classical boundaries at higher energies, seen in the lineout insets, where there is a more abrupt change from higher signal to lower signal as the classical boundary is crossed. Improved agreement here can only be achieved by accounting for correctly treating the coalescing long and short orbit 4 solutions, seen in FIG. 1, in a manner similar to the uniform approximation [73] applied to the equivalent SFA orbit, see e.g., [74].

The high-energy rings visible in FIG. 2(a) [around $(p_{fz}, p_{fy}) = (-2.0, 0.0)$] and FIG. 2(b) [around $(p_{fz}, p_{fy}) = (-2.5, 0.0)$] are particularly well-captured. Previously these have not been very well described by the CQSFA, but now additional orbit 4 contributions have been included that lead to very good agreement. The high-energy rings can be completely attributed to ‘typical’ pairs of orbit 4, where the interference between pairs gives the ring-like interference, previously only the long orbit was included in the CQSFA. In FIG. 2(b), the left most high-energy rings [around $(p_{fz}, p_{fy}) = (-2.5, 0.0)$] can be attributed to the orbit 4 pairs ionized near the peak at 2 cycles (FIG. 1(b)), while the right most high-energy rings [around $(p_{fz}, p_{fy}) = (3.0, 0.0)$] can be attributed to the orbit 4 pairs ionized near the peak at 2.5 cycles, see FIG. 1(b).

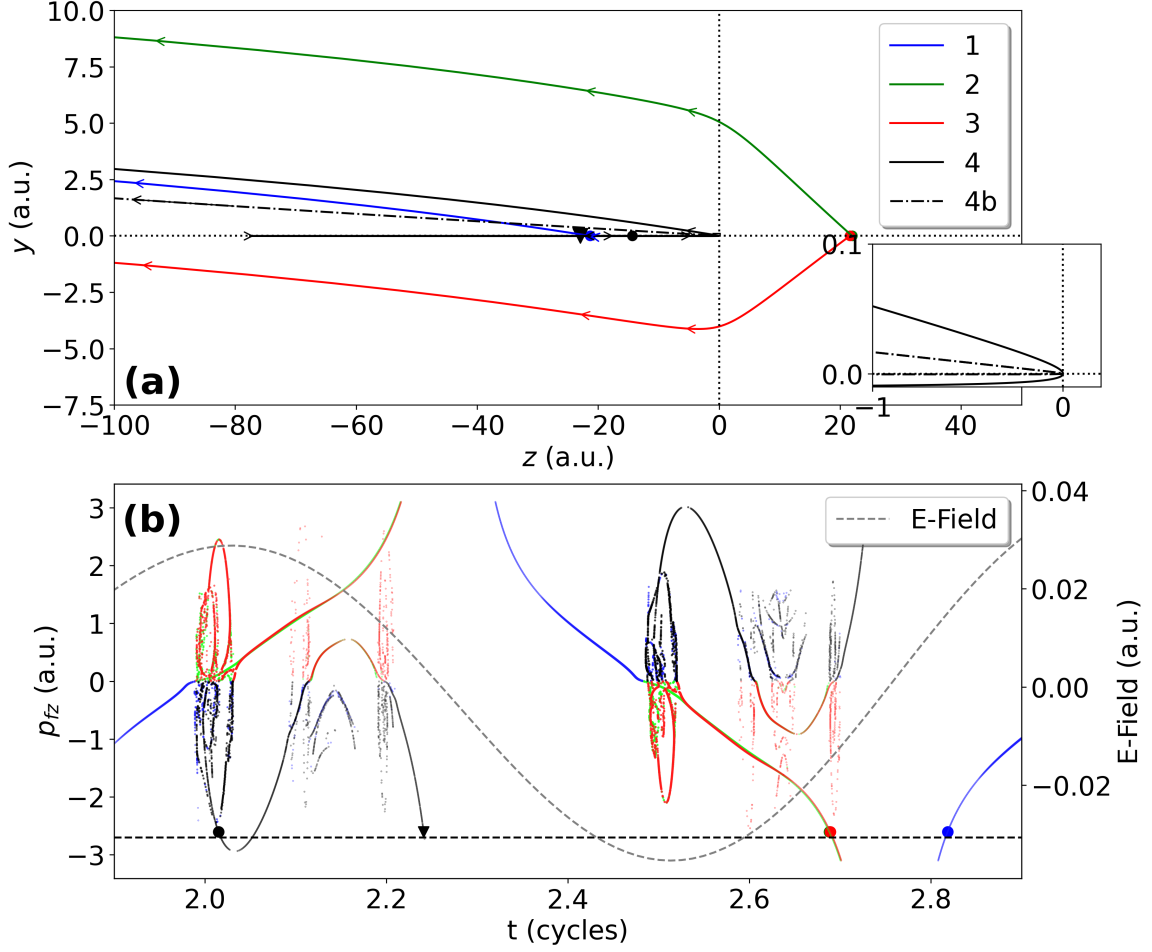


FIG. 1. Example trajectories for all 4 orbits (a), and the times of ionization for different final momenta p_{fz} (b). In the case of orbit 4 two solutions are shown, one “regular” laser driven recollision, and one “directly” recolliding, labelled 4b. The laser is linearly polarized along the z axis. The tunnel exits are marked by circles (triangle for 4b). (a) shows the four orbit types, the y -axis has been stretched to better show the detail. (b) plots the real time of ionization vs the p_z momentum over a single laser cycle, with the 6-cycle electric field superimposed. The ionization target is hydrogen, the laser wavelength is $\lambda = 1600$ nm and the intensity is $I_0 = 5 \times 10^{13}$ W/cm². An inset showing the dynamics of orbit 4 and 4b close to the core is given, with its region marked by the rectangle (a). The final perpendicular momentum is chosen to be $p_{fx} = 0.0$ a.u. $p_{fy} = 0.05$ a.u., while in panel (a) $p_{fz} = -2.704$, which is denoted by the black dashed line in panel (b). Note the ionization times for orbit 2 in (b) are almost the same as those for orbit 3, and thus mostly obscured. The solutions corresponding to the trajectories plotted in (a) are marked on (b) by circles (triangle for 4b) on the dashed line.

The general high level of agreement seen in FIG. 2 validates the CQSFA approach, allowing the use of the trajectory-based machinery for interpretation and to probe the physics in detail. This also provides an easy platform to extend the formalism to include additional effects, such as the spin-orbit coupling during photoelectron recollisions.

In FIG. 3, we plot metrics for five example high-energy rescattered trajectories following ionization of hydrogen for the 6-cycle laser pulse, in preparation for including spin-orbit coupling dynamics, this includes the evolution of the velocity [FIG. 3(a)], distance from the origin [FIG. 3(b)], and the kinetic energy, potential and spin-orbit phase terms in the action [FIG. 3(c)]. We choose

two pairs of rescattered trajectories that are ionized near the field peaks at 2 and 3 laser cycles [see ionization times marked on the laser field in FIG. 3(a)] and recollide around field crossings after $2/3$ to $3/4$ of a cycle of propagation, note this differs from the well-known $2/3$ result [15] due to the inclusion of the Coulomb field. These trajectories are the previously discussed orbit 4 pairs, responsible for the high-energy ring-like structures in FIG. 2. We also include orbit 4b in FIG. 3. As previously mentioned orbit 4b has a low probability, so no clear features are visible in the spectrum in FIG. 2, however, it undergoes a very high-energy recollision so is a useful test case.

Despite employing non-relativistic intensities and all

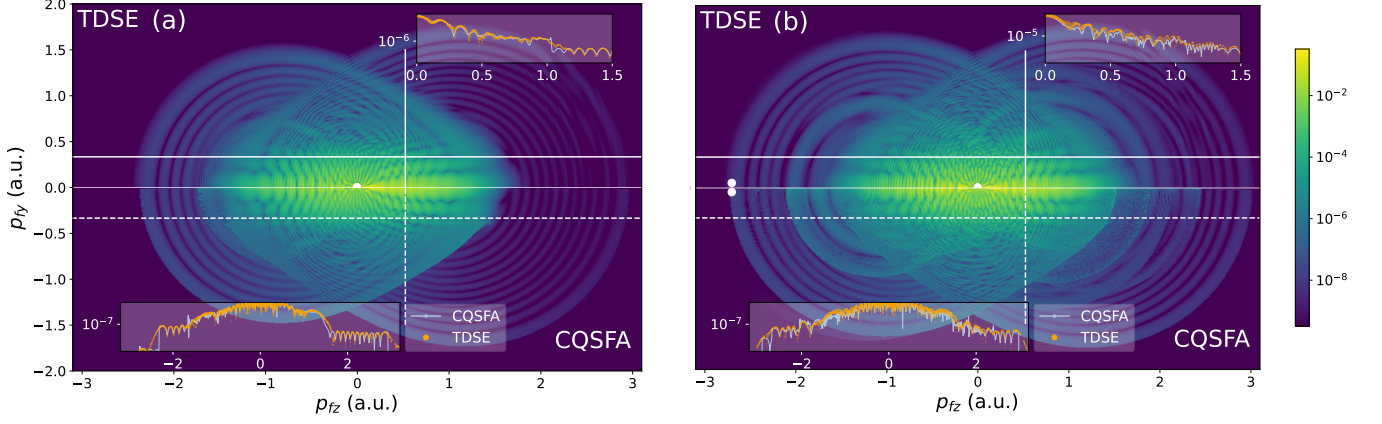


FIG. 2. Comparison of PMDs for strong-field ionization of hydrogen computed using the TDSE and CQSFA, for a 4-cycle and 6-cycle \sin^2 pulse, panels (a) and (b) respectively. The upper half of each panel is computed using the TDSE solver QPROP, while the lower half is computed using the CQSFA. The insets show lineout plots of the TDSE and CQSFA PMDs. With the white horizontal lines showing the region plotted in the bottom insets, and the white vertical lines showing the region plotted in the top insets. The intensity is $I_0 = 5 \times 10^{13}$ W/cm² and wavelength $\lambda = 1600$ nm, the target is hydrogen with $I_p = 0.5$ a.u. The white dots to the left in panel (b) correspond to the example trajectories plotted in Figs. 1 and 3.

final photoelectron speeds being far from relativistic, the momentum transfer during recollision is strongly relativistic. This can be seen in FIG. 3(a), by the large superluminal velocity spikes, occurring during recollisions. The long and short orbit 4 trajectories consistently reach $v \approx 2c$, while for the directly recolliding orbit $v \approx 6c$. These fast speeds are due to how strongly the core is probed, FIG. 3(b) shows that the trajectory's distance from the origin goes below 10^{-5} a.u. Therefore, relativistic considerations have an impact for a sizeable part of the recolliding wavepacket, that, as we will show, noticeably affects the PMD in regions dominated by rescattering. However, these high speeds are only reached for very short time-periods, within a single attosecond. Thus, if it is for such short times, can it be simply neglected?

The phases in FIG. 3(c), where we plot the time-integral of the kinetic energy $K(t)$, potential energy $V(t)$, and spin-orbit interaction $H_{SO}(t)$, see Eq. (12), help us to understand the importance of these very fast speeds over very short time-periods. Given that the atomic core is probed so strongly, a large phase due to spin-orbit coupling is acquired. In the case of the directly recolliding trajectory, the spin-orbit phase (in purple) actually exceeds the phase picked up from the Coulomb potential. This is unexpected and requires careful analysis. It seems likely that these results may be overestimated, while they include trajectories with superluminal speeds. Crucially, the spin-orbit phase only really appreciably changes in the attosecond time-period when superluminal velocities are reached. This can be seen from the highly abrupt change in the dashed-dotted lines in FIG. 3(c).

Overall, in FIG. 2, there is very good agreement with the TDSE, but this is the non-relativistic solutions of the Schrödinger equation, which allows for portions of the wavepacket to travel faster than the speed of light, as we see here. Thus, we can deduce that there is a non-

trivial contribution from rescattered wavepackets, which have a superluminal group velocity. Clearly this is unphysical, and therefore we should go beyond the TDSE and nonrelativistic CQSFA.

IV. FORMULATION OF RELATIVISTIC CQSFA

The results in FIG. 3, show that the most rescattered part of the wavepacket, gains unexpected large velocities, which warrants a relativistic treatment including spin-orbit coupling. The starting point for this is the Dirac equation, but as we are not considering relativistic laser intensities we will consider the expansion of the Dirac equations, up to terms of order $(v/c)^2$ [75]. The laser field may be included through minimal coupling, this gives what is sometimes referred to as the Breit-Pauli Hamiltonian

$$\hat{H}(t) = \frac{1}{2} (\mathbf{p} + \mathbf{A}(\hat{\eta}))^2 + \hat{\mathbf{S}} \cdot \mathbf{B}(\hat{\eta}) - \frac{1}{8c^2} (\hat{\mathbf{p}} + \mathbf{A}(\hat{\eta}))^4 + V(\hat{\mathbf{r}}) - \frac{1}{8c^2} \nabla_{\mathbf{r}}^2 V(\hat{\mathbf{r}}) + \frac{\partial V(|\hat{\mathbf{r}}|)}{2c^2 |\hat{\mathbf{r}}|} \hat{\mathbf{L}} \cdot \hat{\mathbf{S}}, \quad (10)$$

where $\hat{\eta} = \omega t - \mathbf{k} \cdot \hat{\mathbf{r}}$, $\mathbf{A}(\hat{\eta})$ and $\mathbf{B}(\hat{\eta})$, are the magnetic vector potential and magnetic field, respectively, while $\hat{\mathbf{L}} = \hat{\mathbf{r}} \times (\hat{\mathbf{p}} + \mathbf{A}(\hat{\eta}))$ is the angular momenta, $\hat{\mathbf{S}} = \hat{\sigma}/2$ is the spin operator, and $\hat{\sigma} = \sigma_x \hat{x} + \sigma_y \hat{y} + \sigma_z \hat{z}$ is the Pauli vector, constructed from the Pauli matrices.

Given that the wavelength of the laser-field is not too long (or too short) [76] we may apply the dipole approximation, which allows the velocity and length gauge forms

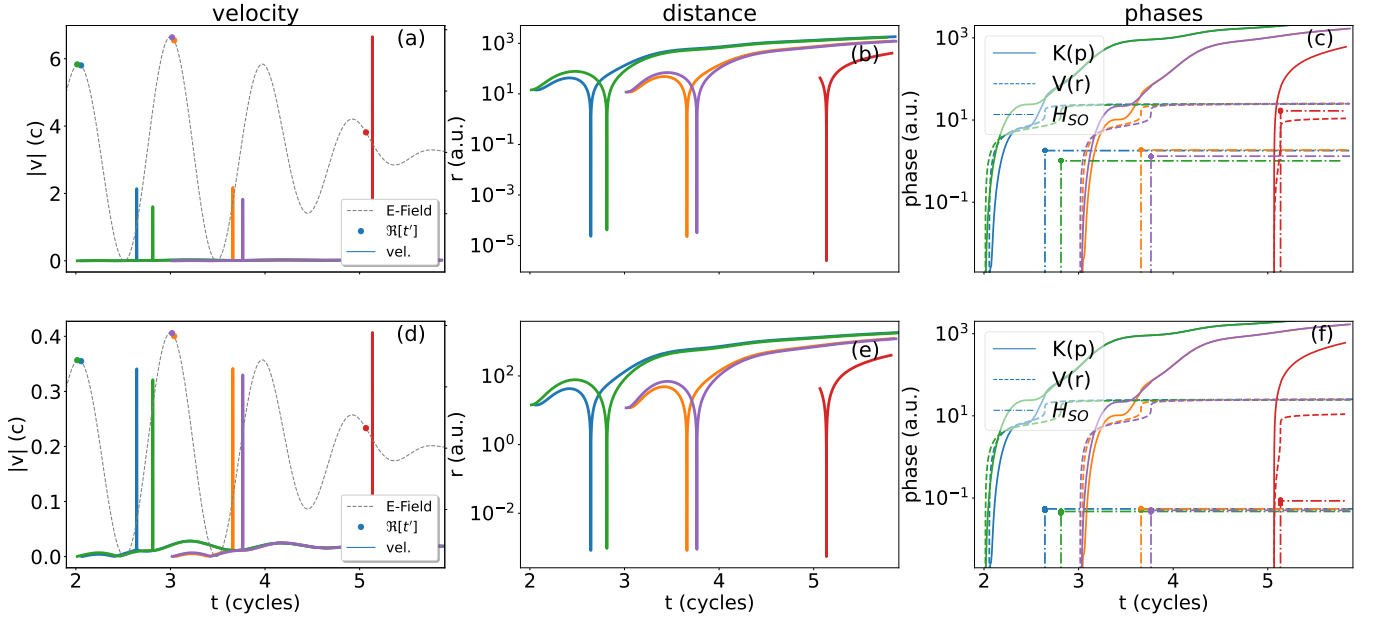


FIG. 3. Examples of velocity transfer and resulting phases picked up of rescattered orbit 4 trajectories, following strong-field ionization of hydrogen. (a) and (d): Velocity over time given by coloured lines (with abrupt spikes at recollisions) with the laser field plotted by a black dashed line, where ionizations times are marked on the field by coloured circles, where the colour of the circle and velocity line corresponds to particular orbits. Blue and green correspond to long and short trajectories with an ionization time around 2 cycles, orange and purple, to long and short trajectories with an ionization time around 3 cycles, and red, to an orbit 4b trajectory with an ionization time around 5 cycles. (b) and (e): Distance over time given by coloured lines, the colours match the same orbits as panel (a). (c) and (f): The phase acquired from kinetic energy $K(p)$ [solid lines], potential energy $U(r)$ [dashed lines], and spin-orbit coupling H_{SO} , see Eqs. (38) and (39), [dot-dashed lines with an abrupt increase during recollision], which is given by the time-integral of these quantities over each trajectory. The approximation to the spin-orbit phase, given by Eq. (42), is plotted in (c) and (f) as coloured circles, as before the colours match the orbits in panel (a). The final momentum of all trajectories is the same as FIG. 1 $\mathbf{p}_f = (0.0, 0.05, -2.704)$, this point is indicated on FIG. 2.

of the Hamiltonian

$$\hat{H}_v(t) = K(\hat{\mathbf{p}}) + U(\hat{\mathbf{r}}) + \mathbf{C}_{SO}(\hat{\mathbf{r}}, \hat{\mathbf{p}}) \cdot \hat{\mathbf{S}} \quad (11)$$

$$\hat{H}_I(t) = \underbrace{K(\hat{\mathbf{p}}) + U(\hat{\mathbf{r}})}_{\hat{H}_0} + \underbrace{\mathbf{C}_{SO}(\hat{\mathbf{r}}, \hat{\mathbf{p}}) \cdot \hat{\mathbf{S}}}_{\hat{H}_{SO}} + \hat{H}_I(t) \quad (12)$$

with

$$K(\hat{\mathbf{p}}) = K_0(\hat{\mathbf{p}}) + K_1(\hat{\mathbf{p}}) = \frac{\hat{\mathbf{p}}^2}{2} - \frac{\hat{\mathbf{p}}^4}{8c^2} \quad (13)$$

$$U(\hat{\mathbf{r}}) = U_0(\hat{\mathbf{r}}) + U_1(\hat{\mathbf{r}}) = V(\hat{\mathbf{r}}) - \frac{\nabla_{\mathbf{r}}^2 V(\hat{\mathbf{r}})}{8c^2} \quad (14)$$

$$\mathbf{C}_{SO}(\hat{\mathbf{r}}, \hat{\mathbf{p}}) = \frac{\partial_r V(|\hat{\mathbf{r}}|)}{2c^2 |\hat{\mathbf{r}}|} \hat{\mathbf{r}} \times \hat{\mathbf{p}} \quad (15)$$

and $\hat{H}_I(t) = \mathbf{E}(t) \cdot \hat{\mathbf{r}}$ and $\hat{\mathbf{p}} = \hat{\mathbf{p}} + \mathbf{A}(t)$. The relativistic correction terms to the kinetic and potential energy (the Dyson correction), $K_1(\hat{\mathbf{p}})$ and $U_1(\hat{\mathbf{r}})$, still permit the solution given in Eq. (5), as here we assumed general forms for the kinetic and potential energy. The spin and spin-orbit coupling can, however, not be treated through the same path-integral approach that we used before, as we must consider the additional spin degree of freedom and coupling between them. In fact, historically

a proper treatment of spin by path-integrals took some time to develop. In order to describe spin in a path-integral framework, we require a mapping of the spin to a continuous variable. The treatment of spin in terms of so-called coherent spin-states (an irreducible representation for $SU(2)$) [77, 78] does just this. The mapping is achieved through the coherent spin states, defined as

$$|z\rangle = \frac{|\downarrow\rangle + z|\uparrow\rangle}{\sqrt{1 + |z|^2}}, \quad (16)$$

with further details given in Appendix B. These states map spin states to the complex plane, see FIG. 4. Some key values are $|z \rightarrow 0\rangle = |\downarrow\rangle$, $|z \rightarrow \infty\rangle = |\uparrow\rangle$, $|z \rightarrow 1\rangle = |+\rangle$ and $|z \rightarrow -1\rangle = |-\rangle$. We may write an initial-fine-structure state [79], with quantum numbers j , and m_j , and energy E_{jm_j} as

$$|\Phi_{jm_j}\rangle = \sum_m f_{lm}^{jm_j} |z_{lm}^{jm_j}\rangle \otimes |\psi_{lm}\rangle \quad (17)$$

with $f_{lm}^{jm_j} = C_{lm, \frac{1}{2} - \frac{1}{2}}^{jm_j} \sqrt{1 + |z_{lm}^{jm_j}|^2}$, $z_{lm}^{jm_j} = C_{lm, \frac{1}{2} - \frac{1}{2}}^{jm_j} / C_{lm, \frac{1}{2} - \frac{1}{2}}^{jm_j}$ and $C_{lm, S m_s}^{jm_j} = \langle l, S; m, m_s | l, S; j, m_j \rangle$ are Clebsch-Gordon coefficients.

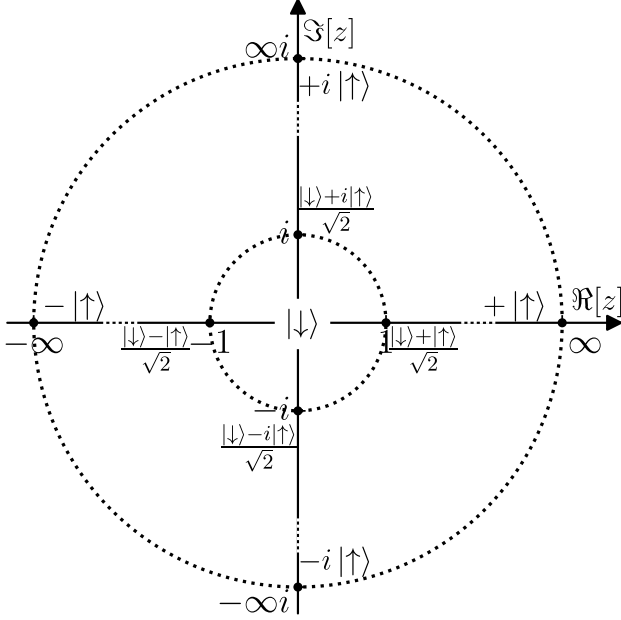


FIG. 4. The mapping of the complex plane to coherent spin states $|z\rangle$, given by Eq. (16). Some key values are marked by black dots and their corresponding states are given by adjacent labels.

The transition amplitude can be defined for ionization starting in a specific bound state $|\Phi_{jm_j}\rangle$ with quantum numbers j and m_j and energy E_{jm_j} , and finishing in a continuum spin-state $|\psi_{\mathbf{p}}, z\rangle = |\psi_{\mathbf{p}}\rangle \otimes |z\rangle$, at $t \rightarrow \infty$. The amplitude is then given by

$$\begin{aligned} M(\mathbf{p}, z) &= \langle \psi_{\mathbf{p}}, z | U(t, t_0) | \Phi_{jm_j} \rangle \\ &= -i \int_{-\infty}^t dt' \langle \psi_{\mathbf{p}}, z | U(t, t') H_I(t') | \Phi_{jm_j} \rangle e^{-iE_{jm_j}t'}. \end{aligned} \quad (18)$$

As before, we insert the resolution of the identity $\mathbf{1}_3 = \int d^3\tilde{\mathbf{p}}_0 |\tilde{\mathbf{p}}_0\rangle \langle \tilde{\mathbf{p}}_0|$, where $\tilde{\mathbf{p}}_0 = \mathbf{p}_0 + \mathbf{A}(t')$

$$\begin{aligned} M(\mathbf{p}, z) &= -i \int_{t_0}^t dt' \int d^3\tilde{\mathbf{p}}_0 \langle \psi_{\mathbf{p}}, z | U(t, t') | \tilde{\mathbf{p}}_0 \rangle \\ &\quad \times \langle \tilde{\mathbf{p}}_0 | \hat{H}_I(t') | \Phi_{jm_j} \rangle e^{-iE_{jm_j}t'}. \end{aligned} \quad (19)$$

To proceed, we must expand the spin state, so we can exploit the fact that $[\hat{H}_I(t), \hat{\mathbf{S}}] = 0$.

$$\langle \tilde{\mathbf{p}}_0 | \hat{H}_I(t') | \Phi_{jm_j} \rangle = \sum_m |z_{lm}^{jm_j}\rangle d_m(\tilde{\mathbf{p}}_0, t') \quad (20)$$

with $d_m(\mathbf{p}_0, t') = f_{lm}^{jm_j} \langle \mathbf{p}_0 | \hat{H}_I | \psi_{lm} \rangle$. Now the transition amplitude may be written

$$M(\mathbf{p}, z) = -i \sum_m \int_{-\infty}^t dt' \mathcal{K}_m(\mathbf{p}, z) e^{-iE_{jm_j}t'}, \quad (21)$$

where

$$\mathcal{K}_m(\mathbf{p}, z) = \int d^3\tilde{\mathbf{p}}_0 \langle \psi_{\mathbf{p}}(t), z | U(t, t') | \tilde{\mathbf{p}}_0, z_{lm}^{jm_j} \rangle d_m(\tilde{\mathbf{p}}_0, t'). \quad (22)$$

Now we are in a position to utilize the path-integral formalism for a particle with spin [78, 80–82] and obtain

$$\begin{aligned} \mathcal{K}_m(\mathbf{p}, z) &= \\ &\int \frac{\mathcal{D}'\mathbf{r}}{(2\pi)^3} \int_{\mathbf{r}_0}^{\mathbf{p}_f} \mathcal{D}'\mathbf{p} \int_{z_{lm}^{jm_j}}^z \mathcal{D}\mu(z) d_m(\mathbf{p}_0, t') e^{i\mathcal{A}[\mathbf{r}, \mathbf{p}, z, t']}. \end{aligned} \quad (23)$$

Here it is possible to solve the functional integral over z analytically. We take advantage of this fact and rewrite Eq. (23) as

$$\begin{aligned} \mathcal{K}_m(\mathbf{p}, z) &= \\ &\int \frac{\mathcal{D}'\mathbf{r}}{(2\pi)^3} \int_{\mathbf{r}_0}^{\mathbf{p}_f} \mathcal{D}'\mathbf{p} \mathcal{M}_{\text{SO}}^m(\mathbf{r}, \mathbf{p}, z, t') d_m(\tilde{\mathbf{p}}_0, t') e^{iS[\mathbf{r}, \mathbf{p}, t']} \end{aligned} \quad (24)$$

with

$$\begin{aligned} \mathcal{M}_{\text{SO}}^m(\mathbf{r}, \mathbf{p}, z, t') &= \\ &\frac{a^*(t) - b^*(t) z_{lm}^{jm_j*} + b(t)z + a(t)z^* z_{lm}^{jm_j}}{\sqrt{1 + |z|^2} \sqrt{1 + |z_{lm}^{jm_j}|^2}}. \end{aligned} \quad (25)$$

and

$$S[\mathbf{r}, \mathbf{p}, t'] = -E_{jm_j}t' - \int_{t'}^t d\tau (\dot{\mathbf{p}} \cdot \mathbf{r} + H_0[\mathbf{r}, \mathbf{p} + \mathbf{A}(\tau)]). \quad (26)$$

In Eq. (25) $a(t)$ and $b(t)$, are time-dependent functions determined by an ordinary differential equation given the appendix C1 in Eq. (C9). Thus, Eq. (24) may be solved using the saddle-point equations given by Eqs. (6) and (7), leading to the final expression for the transition amplitude

$$\begin{aligned} M(\mathbf{p}, z) &= \\ &= -i \sum_{m,s} C_m(\mathbf{r}_s, \mathbf{p}_s, t_s) \mathcal{M}_{\text{SO}}^m(\mathbf{r}_s, \mathbf{p}_s, z, t_s) e^{iS[\mathbf{r}_s, \mathbf{p}_s, t_s]} \end{aligned} \quad (27)$$

with

$$C_m(\mathbf{r}_s, \mathbf{p}_s, t_s) = \sqrt{\frac{2\pi i}{\partial^2 S / \partial t'^2}} \frac{e^{-i\pi\nu/2}}{\sqrt{|J|}} d_m(\tilde{\mathbf{p}}_{0s}, t_s). \quad (28)$$

Note that this formulation assumes that $\mathcal{M}_{\text{SO}}^m$ varies slowly enough so that it does not affect the saddle-point equation for \mathbf{r}_s and \mathbf{p}_s , which is the weak-coupling limit. Full details of the weak-coupling limit and how we may go beyond it are given in Appendix C1 and C2, respectively.

V. OBSERVABLES AND ANALYTICAL CONSIDERATIONS

A. Spin Measurement

So far we have only considered the case where the final spin is measured and the initial spins are aligned. Now we consider an ensemble of unaligned initial spins and the effect of averaging over final spins. We will use the notation $\mathcal{P}_{i;j}(\mathbf{p})$ or $\mathcal{P}_i(\mathbf{p}; |j\rangle)$ for the probability amplitude given initial spin $j \in [\uparrow, \downarrow]$ and final spin $i \in [\uparrow, \downarrow]$ and momentum $\mathbf{p} \in \mathbb{R}^3$. For averages over initial, final and both spins, we will use $\mathcal{P}_{i;}, \mathcal{P}_{;j}(\mathbf{p})$, and $\mathcal{P}_{; }(\mathbf{p})$, respectively.

Firstly, we will average incoherently over initial spin orientations, for simplicity we will continue with the case of hydrogen. In this case, the spin state $|\Phi_{0\pm 1/2}\rangle = |z_{00}^{\pm 1/2}\rangle |\psi_{00}(t')\rangle$, where either $z_{00}^{-1/2} \rightarrow 0$ (spin down) or $z_{00}^{+1/2} \rightarrow \infty$ (spin up). Spatial rotations of the initial state can cover all possible values of the initial z_{00} . We can show this explicitly by integrating over the Euler angles

$$\mathcal{P}_{\uparrow; }(\mathbf{p}) = \frac{1}{8\pi^2} \int_0^{2\pi} d\alpha \int_0^\pi d\beta \int_0^{2\pi} d\gamma \sin(\beta) \mathcal{P}_{\uparrow}(\mathbf{p}; \mathcal{R}_{\alpha\beta\gamma} |\uparrow\rangle) \quad (29)$$

This is a well-known result but in the Appendix D we show how to do this using coherent spin states, the result is

$$\mathcal{P}_{\uparrow; }(\mathbf{p}) = \frac{1}{2} (\mathcal{P}_{\uparrow;\uparrow}(\mathbf{p}) + \mathcal{P}_{\uparrow;\downarrow}(\mathbf{p})). \quad (30)$$

By the same logic $\mathcal{P}_{\downarrow; }(\mathbf{p}) = \frac{1}{2} (\mathcal{P}_{\downarrow;\uparrow}(\mathbf{p}) + \mathcal{P}_{\downarrow;\downarrow}(\mathbf{p}))$.

If we do not measure spin, the positive operator valued measurement (POVM) is given by $\rho = \frac{1}{2}(|\downarrow\rangle\langle\downarrow| + |\uparrow\rangle\langle\uparrow|)$. This may be applied to a state where the spins are initially prepared to give $\mathcal{P}_{; \uparrow} = \frac{1}{2} (\mathcal{P}_{\uparrow;\uparrow} + \mathcal{P}_{\downarrow;\uparrow})$ and $\mathcal{P}_{; \downarrow} = \frac{1}{2} (\mathcal{P}_{\uparrow;\downarrow} + \mathcal{P}_{\downarrow;\downarrow})$. If we instead apply the POVM to unaligned spins, we obtain the following probability $\mathcal{P}_{; }(\mathbf{p}) = \frac{1}{2} (\mathcal{P}_{\uparrow; }(\mathbf{p}) + \mathcal{P}_{\downarrow; }(\mathbf{p})) = \frac{1}{4} (\mathcal{P}_{\uparrow;\uparrow} + \mathcal{P}_{\uparrow;\downarrow} + \mathcal{P}_{\downarrow;\uparrow} + \mathcal{P}_{\downarrow;\downarrow})$.

In order to isolate the effect of spin, we define a parameter that could feasibly be measured in experiment. This is $\Delta\mathcal{P}_{;\uparrow x}(\mathbf{p})$, defined as the difference between spin initially aligned in the x -direction and unaligned spins given by the difference between spins aligned in the x -direction vs fully unaligned spins, denoted $\mathcal{P}_{\uparrow x}(\mathbf{p})$ and $\mathcal{P}_{; }(\mathbf{p})$, respectively. In the z -basis these probabilities may be written as

$$\begin{aligned} \mathcal{P}_{;\uparrow x}(\mathbf{p}) &= \frac{1}{4} |M_{\uparrow z;\uparrow z}(\mathbf{p}) + M_{\uparrow z;\downarrow z}(\mathbf{p})|^2 \\ &+ \frac{1}{4} |M_{\downarrow z;\uparrow z}(\mathbf{p}) + M_{\downarrow z;\downarrow z}(\mathbf{p})|^2 \end{aligned} \quad (31)$$

and

$$\begin{aligned} \mathcal{P}_{; }(\mathbf{p}) &= \\ \frac{1}{4} (|M_{\uparrow z;\uparrow z}|^2 + |M_{\uparrow z;\downarrow z}|^2 + |M_{\downarrow z;\uparrow z}|^2 + |M_{\downarrow z;\downarrow z}|^2). \end{aligned} \quad (32)$$

Now the difference can be expressed as

$$\begin{aligned} \Delta\mathcal{P}_{;\uparrow x}(\mathbf{p}) &= \mathcal{P}_{;\uparrow x}(\mathbf{p}) - \mathcal{P}_{; }(\mathbf{p}) \\ &= \frac{1}{2} \text{Re}[M_{\uparrow z;\uparrow z}(\mathbf{p}) M_{\uparrow z;\downarrow z}^*(\mathbf{p})] \\ &+ \frac{1}{2} \text{Re}[M_{\downarrow z;\uparrow z}(\mathbf{p}) M_{\downarrow z;\downarrow z}^*(\mathbf{p})]. \end{aligned} \quad (33)$$

This provides an ‘interference’ term due to the fact that spin aligned in the x -axis but we expressed in terms of the z -basis. This provides an observable that is linear in terms of the spin-flip amplitude. The difference term in Eq. (33) may be written more clearly by expanding the transition amplitudes in terms of the sum over saddle points

$$M_{\uparrow z;\uparrow z} = -i \sum_s C_s a_s e^{iS_s} \quad (34)$$

$$M_{\uparrow z;\downarrow z} = -i \sum_s C_s b_s e^{iS_s}, \quad (35)$$

where the subscript s refers to the saddle-point solution being summed over, the spin-orbit amplitude \mathcal{M}_{SO} (Eq. (25)) has been replaced by the coefficient a_s or b_s , while C_s is the prefactor defined in Eq. (28). The arguments \mathbf{p} , \mathbf{r} , t and z have been dropped from a_s , b_s and C_s for simplicity. Thus, the difference can be determined entirely by products of a and b . In the next section, we will solve the equations for a and b analytically to better understand the behaviour of Eq. (33).

B. Analytical Results

In this section we will consider some analytical results, firstly we will solve the equations of motion for the spin dynamics and secondly derive an approximate analytic approximation to the spin-orbit action. As we are using the weak approximation in this work, see Sec. IV, the electron trajectories are unaffected by spin-orbit coupling and retain cylindrical symmetry. Furthermore, we restrict our analysis to the y - z plane, which means the trajectories will only have angular momentum in the x -direction, with $L_z = L_y = 0$, the spin-orbit equations in the weak-coupling limit greatly simplify. The coefficients $a(t)$ and $b(t)$, that enter Eq. (25) and parameterize the spin dynamics, see Eq. (C9), can be found analytically (see Appendix E for derivation). The parameter responsible for spin conserving transitions, is given by

$$\begin{aligned} a(t) &= \cos(S_{\text{SO}}) \text{ and the parameter for spin-flips} \\ b(t) &= -i \sin(S_{\text{SO}}), \end{aligned} \quad (36)$$

where the term S_{SO} that we will refer to as the spin-orbit action is given by

$$S_{\text{SO}} = \int_{\text{Re}[t']}^t d\tau H_{\text{SO}}(\tau) \quad (37)$$

with

$$H_{\text{SO}}(\tau) = \mathbf{C}_{\text{SO}}(\mathbf{r}, \mathbf{p}) \cdot \mathbf{n}(z) \quad (38)$$

and

$$\mathbf{C}_{\text{SO}} = \frac{\frac{\partial}{\partial \mathbf{r}} V(|\mathbf{r}|)}{2c^2 |\mathbf{r}|} \mathbf{L}. \quad (39)$$

Here $\mathbf{n}(z) = (n_1, n_2, n_3)$, $n_1 + in_2 = 2z^*/(1 + |z|^2)$, $n_3 = -(1 - |z|^2)/(1 + |z|^2)$ and $\mathbf{L} = \mathbf{r} \times \mathbf{p}$.

The weak-coupling approximation requires that the spin-orbit action S_{SO} is much smaller than the remaining action S . This means that a and b can be expanded in a power series of S_{SO} , such that $a(t) \approx 1$ and $b(t) \approx -iS_{\text{SO}}$. Hence, spin-flip probability will be quadratic in S_{SO} and may be neglected $|M_{\uparrow z; \downarrow z}|^2 \approx 0$ to linear order, which may be expected for the small spin-orbit coupling of hydrogen. However, the difference term given by Eq. (33) has mixed terms like ab^* and will be of linear order in S_{SO} and so some effect whereby different alignment of spin affect the final probability distribution is expected.

The spin-orbit action term S_{SO} can be accurately approximated by assuming contributions only occur when the trajectory is very close to the origin and undergoing Coulomb dominated dynamics, see FIG. 3. Thus, during the recollision it is an accurate approximation to neglect the laser field and assume the trajectories follow Kepler hyperbolae, or when including relativistic corrections to the kinetic energy, the trajectories will follow relativistic corrected Kepler hyperbolae [83], which for a $-Z/r$ potential takes the form

$$\frac{1}{r} = \bar{C}_0 (1 + \bar{e} \cos(\bar{\kappa}(\theta - \theta_c))), \quad (40)$$

where $\bar{C}_0 = (1 + \frac{1}{2}\epsilon)(Z/l^2)$, $\bar{\kappa} = 1 - \frac{1}{2}\epsilon$, with the corrected eccentricity $\bar{e} = (1 + \frac{1}{2}\epsilon)e$ written in terms of the Kepler eccentricity $e = \sqrt{1 + 2El^2/Z^2}$, with E being the energy and l the magnitude of the angular momentum in the non-relativistic case. The relativistic correction parameter $\epsilon = 1/(\bar{l}^2 c^2)$, where the magnitude of the relativistic angular momentum $\bar{l} \approx l(1 + v^2/c^2)$. In the case without relativistic corrections to the kinetic energy $\epsilon = 0$. The spin-orbit action S_{SO} , given in Eq. (37), may be written more explicitly as

$$S_{\text{SO}} = \frac{Z}{2c^2} \int_{\text{Re}[t']}^t \frac{\bar{l} d\tau}{r^3}, \quad (41)$$

by substituting the integration variable from time t to the orbital angle θ via $r^2 d\theta = \bar{l} d\tau$ and substituting in

Eq. (40) the spin-orbit action can be approximated as

$$S_{\text{SO}} \approx \frac{\bar{C}_0}{2c^2} \left(\arccos\left(-\frac{1}{\bar{e}}\right) + \frac{\bar{e}}{\bar{\kappa}} \sqrt{1 - \frac{1}{\bar{e}^2}} \right). \quad (42)$$

This equation is tested in FIG. 3, using the position and velocity when the recolliding trajectory first reaches a distance of 1 a.u. from the residual ion, the value of the spin-orbit action phase, S_{SO} , is computed and placed on the figure as the circles in panels (c) and (f). This works exceptionally well for the non-relativistic case [FIG. 3(c)], with no difference visible between it [coloured circle] and the numerical value [dot-dashed line]. It also works well for the case including relativistic correction to the kinetic energy [FIG. 3(f)], however, the approximated value (represented by a circle) is slightly off the numerical value (plotted as a dot-dashed line), indicating the analytical estimation slightly worsens in the relativistic case.

VI. RELATIVISTIC RESULTS

The trajectories involved in the relativistic computation are shown in the bottom row of FIG. 3. With relativistic corrections to the kinetic energy, the velocity of the rescattered trajectories, FIG. 3(d), no longer exceeds the speed of light. There is also a directly related effect on the minimum distance to the core, FIG. 3(e), which is reduced by more than two orders of magnitude compared to the non-relativistic case in FIG. 3(b). We can gain insight into why the core is probed less strongly when relativistic corrections are included, by examining the problem from a non-relativistic perspective. We may imagine that there is an effective ‘repulsion’ (dependent on the velocity), which balances the attraction of the Coulomb potential, meaning that the electron does not get so close to the core, only reaching around 10^{-3} a.u. This effect can be seen clearly by rearranging the saddle point equations of motion (neglecting the laser field) to give

$$\ddot{\mathbf{r}} = (\mathbf{1}_3 - \frac{1}{2c^2} \underline{\underline{M}}) \mathbf{F}, \quad (43)$$

where $\mathbf{F} = -\nabla V(\mathbf{r})$ is the classical non-relativistic force due to the potential and $\underline{\underline{M}}$ is a matrix given by $\underline{\underline{M}} = \mathbf{1}_3 \mathbf{p}^2 + 2\mathbf{p} \otimes \mathbf{p}$. For a derivation of Eq. (43), see Appendix F. Now it is possible to see, following Appendix F, that for a trajectory with momentum \mathbf{p} confined to the z -axis, the attractive force of the potential is reduced by the factor $1 - \frac{3}{2} \frac{v^2}{c^2}$, while for circular motion with momentum perpendicular to the origin this factor becomes $1 - \frac{1}{2} \frac{v^2}{c^2}$. In both cases, this leads to trajectories that do not probe the core as closely as in the non-relativistic case. The result of the significant increase in the minimal distance from the core and the reduction in the velocity is that the spin-orbit action phase term is greatly reduced, by an

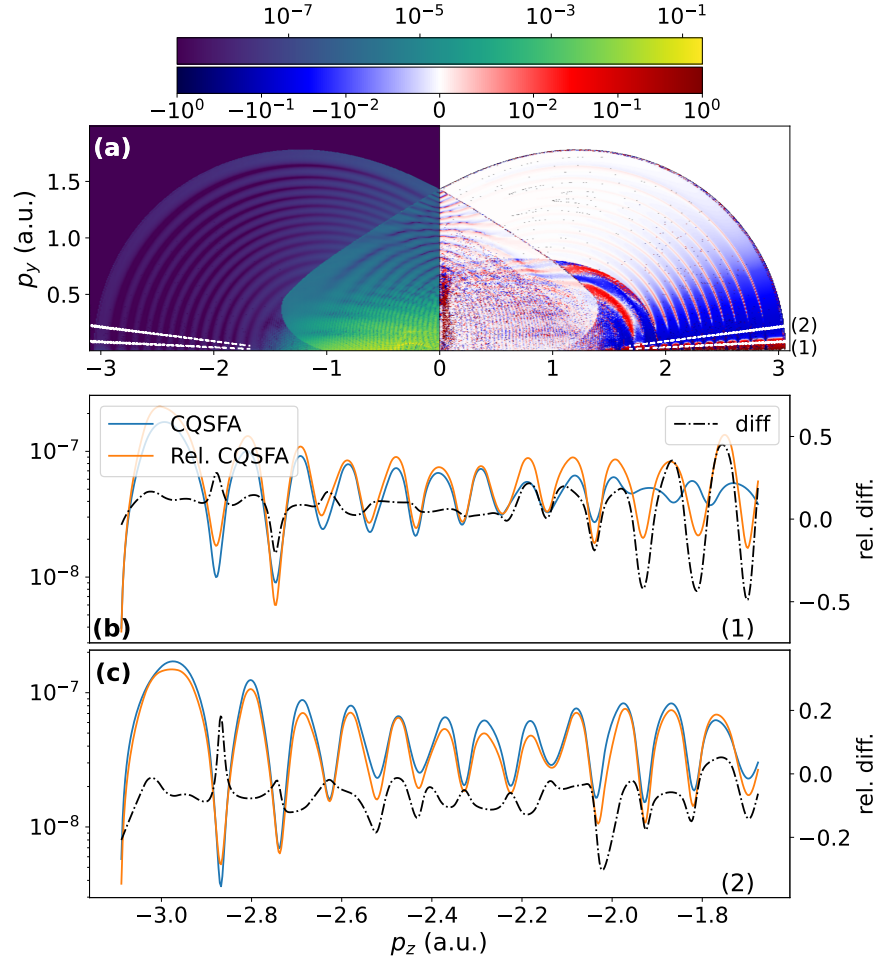


FIG. 5. The difference between momentum distributions with and without relativistic corrections. Spin and spin-orbit effect have been neglected by setting the $\mathcal{M}_{SO} = 1$ in Eq. (27). (a) left is the relativistic momentum distribution for a hydrogen target, averaged over initial and final spins, $\mathcal{P}_i(\mathbf{p})$ of Eq. (32). (a) right is the difference between this and the distribution without relativistic corrections to the kinetic energy. (b) and (c) include a lineout of (a) left [solid line left] and (a) right [dashed right], given by the lower [labelled (1)] and upper [labelled (2)] white lines in (a), respectively.

order of magnitude for the directly recolliding trajectory and by over a factor of 5 for the long and short trajectory pairs, and the phase for all trajectories are over an order of magnitude below the phase due to the Coulomb potential. Thus, without relativistic corrections to the kinetic energy, the spin-orbit coupling phase is overestimated by around an order of magnitude, while with relativistic corrections, spin-orbit coupling is quite modest. The relatively small action phase of the spin-orbit coupling, in this case, also validates the weak-coupling approach used in the relativistic CQSFA of Sec. IV.

Another important observation that was already discussed in V is that the analytical approximation for the spin-orbit phase, given by Eq. (42), provides a very good approximation when compared to the numerical value, in FIGS. 3(c) and (f), for the case without and with the kinetic energy corrections, respectively.

In FIG. 5, we show the PMD for a linearly polarized monochromatic laser field, where ionization is al-

lowed only during a single cycle. The target is hydrogen as before and the intensity and wavelength are again 5×10^{13} W/cm² and 1600 nm, respectively. The consideration of a single cycle provides a simple PMD, with fewer trajectories for an easier analysis, while also maximizing the rescattered trajectories' return energy, thus, showing the largest relativistic effects. Similar results can still be seen for relativistic computations using a \sin^2 envelope (not shown). In this figure, we have neglected the spin and spin-orbit effect to isolate the kinetic energy corrections, $K_1(\hat{\mathbf{p}})$ in Eq. (13). The left side of FIG. 5(a) plots the PMD including relativistic corrections to the kinetic energy, where the same high-energy rings (p_{fz}, p_{fy}) $\approx (-3.0, 0.1)$ a.u. can be seen as in FIG. 2(a). The right side of FIG. 5(b), shows the normalized difference between the CQSFA with and without relativistic kinetic energy corrections. We find that in the high-energy rescattering region near the p_z -axis a series of red peaks occur, which shows that the CQSFA

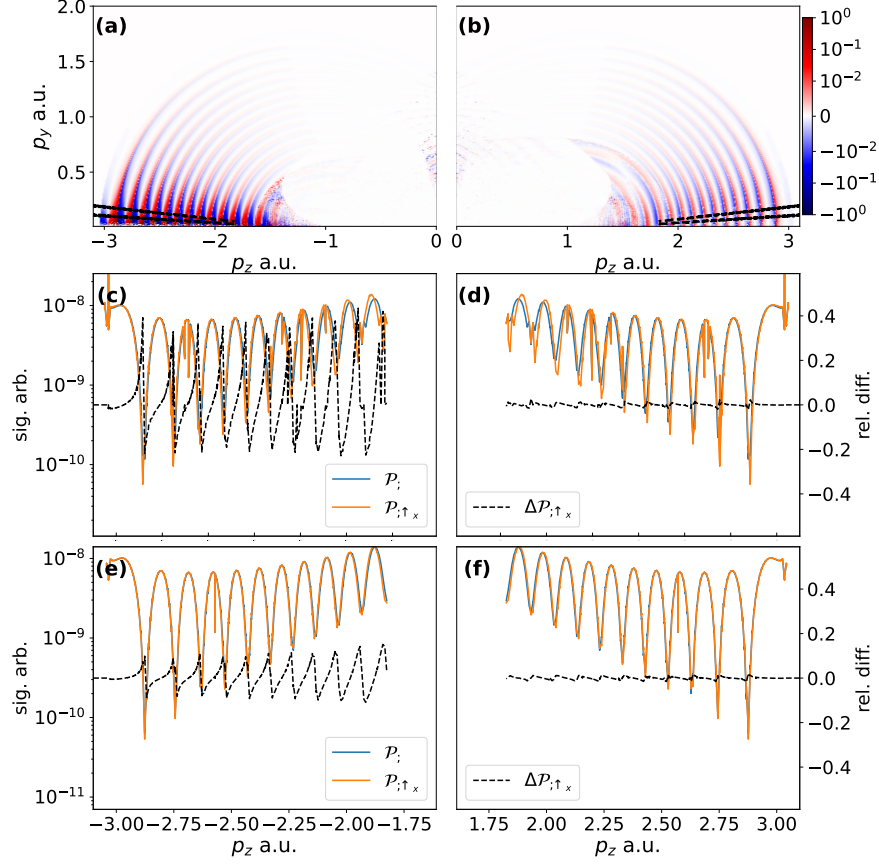


FIG. 6. The difference between momentum distributions with initial spin aligned in the x -direction and totally averaged spins, given by $\Delta\mathcal{P}_{i;\uparrow x}(\mathbf{p})$ defined in Eq. (33). The left column [(a), (c), (e)] neglects the corrections the kinetic energy, the right column [(b), (d), (f)] includes corrections to the kinetic energy. (a) and (b) show the signal of averaged spins $\mathcal{P}_i(\mathbf{p})$ and x -aligned spins $\mathcal{P}_{i;\uparrow x}(\mathbf{p})$, and relative difference $\Delta\mathcal{P}_{i;\uparrow x}(\mathbf{p})$. As in FIG. 5, the lower lineout in (a) [(b)] corresponds to (c) [(d)], while the upper lineout corresponds to (e) [(f)].

PMD signal with relativistic kinetic energy corrections is larger than without. However, away from the p_z -axis this situation reverses. In FIGS. 5(b) and (c), we look at these regions in more detail by plotting the lineouts, marked on panel (a). The first lineout, near the axis (b), clearly shows that the relativistic case exceeds the non-relativistic case, with the normalized difference exceeding 50%. While the situation is reversed in FIG. 5(c) and the normalized difference approaches 20%.

The main driver of this effect is an overall change in probability for the pair of rescattered trajectories that contribute to this region. This is because scattering with and without relativistic corrections only appreciably changes $\mathbf{p}_{0\perp}$, the initial momentum perpendicular to the laser polarization direction, which leaves the ionization times and tunnelling probability almost the same with and without relativistic corrections to the kinetic energy. The case with relativistic corrections leads to a larger value of initial perpendicular momentum $|\mathbf{p}_{0\perp}|$ than the non-relativistic case. The perpendicular momentum controls how close the electron trajectory gets to the ion,

with a higher value meaning the core gets probed less strongly in the case with relativistic corrections.

These changes in initial conditions affect the so-called stability factor $1/\sqrt{|J|}$, determined from the Jacobian by $J = \frac{\delta\mathbf{p}_f}{\delta\mathbf{p}_0}$ in Eq. (5), see also Eq. (28), which leads to the visible changes in the PMDs. In the case of backscattering, where the scattering angle is nearly 180° , the trajectories for the case including kinetic energy correction undergo a much smaller momentum change than those without the kinetic energy corrections. This means they are less sensitive to the initial conditions. On the other hand, for scattering angles less than approximately 175° , the trajectories including relativistic corrections have a comparable momentum transfer to those without the corrections. However, relativistic scattering can lead to a greater scattering angle than the completely non-relativistic case, meaning now the trajectories including relativistic corrections to the kinetic energy are more sensitive to the initial conditions than the case without corrections.

Now we will consider the effect of spin-orbit coupling.

It is important to note that in this article we only consider the final electron momentum in the p_{fz} - p_{fy} plane, and the equations of motion for the electron are cylindrically symmetric [84]. Thus, the trajectories are restricted to the zy -plane, and the angular momentum is in the x -direction and couples to spin in this direction. For motion in rotated planes, e.g., the p_z - p_x plane the angular momentum and spin-orbit coupling will be rotated accordingly.

In FIG. 6, the effect of spin-orbit coupling is considered on the initial alignment of the electronic spin. FIG. 6(a) shows the relative difference between electronic spin aligned in the positive x -direction vs unaligned spins, where relativistic kinetic energy corrections have been neglected. This combination of spin alignment is considered, as it could be feasibly done in experiment and measured, using a B-field for spin alignment. Lineouts near the p_z -axis are shown in panels (c) and (e) (the same as in FIG. 5, where the largest effect, due to the backscattered trajectories, can be observed). Here, the relative difference approaches 50%, this is surprising given the small degree of spin-orbit coupling expected for a hydrogenic target, and this difference could foreseeably be measured.

As argued above, a correct treatment requires that corrections to the kinetic energy be taken into account, so we plot the same in FIG. 6(b), (d), and (f) but include these corrections. This leads to much weaker differences, demonstrating the importance of including the relativistic kinetic energy correction for the rescattered electron when considering spin-orbit coupling. The difference with and without the relativistic kinetic energy corrections can be explained by the behaviour of in the spin-orbit phase, which is far too big if kinetic energy corrections are not taken into account, see FIG. 3.

VII. NEW LIMIT ON NON-RELATIVISTIC THEORIES

The results from Sec. VI highlight the importance of relativistic corrections for the rescattered portion of the wavepacket in strong-field ionization. However, commonly employed estimations for when relativistic effects should be accounted for in the infrared regime rely on classical arguments considering the motion of the free electron in the continuum [27, 76] and do not account for scattering. In this section, limits will be derived that account for the scattering behaviour and we will compare to existing limits.

A commonly employed limit for relativistic behaviour is when the ponderomotive energy approaches the electron rest mass energy, that is $U_p = mc^2/2$ [76], this leads to a condition on the intensity $I_0 = 2c^2\omega^2$ above which relativistic effects are significant. This is plotted as blue dashed line in the upper left corner of FIG. 7(b), the blue dot indicates the parameters used here are well below this intensity. Another important condition is the region

where the dipole approximation is valid, this is given by an ‘upper’ and ‘lower’ limit. The ‘upper’ limit is simply that the angular frequency needs to be small enough and is given by $\omega = 1/2$ [76]. The ‘lower’ limit derives from the requirement that the motion of the free electron due to the laser magnetic field should be small and leads to the following limit on intensity $I_0 = 8c\omega^3$, where higher intensities mean the break-down of the dipole approximation. These upper and lower limits are given by the red solids lines in FIG. 7(b). A slightly smaller region, where tunnelling models will hold, is also given by the blue dotted lines in FIG. 7(b), see [76].

To derive a new condition, we must consider the maximum velocity that a rescattering trajectory will achieve given specific laser parameters and particular scattering angle. We will consider angles close to backscattered, as these represent the most extreme cases. The most energetic rescattered trajectories gain around $3.17U_p$ kinetic energy from the laser field upon return. If we assume once the electron is close enough, r_B from the core, it undergoes Coulomb dominated dynamics, and we may ignore the field from this point, then an energy conservation argument may be used to approximate the maximum velocity. The total energy entering this boundary may be approximated as $E_B = 3.17U_p - Z/r_0$, where the potential energy convert to kinetic energy from the tunnel exit at r_0 , to the boundary (r_B) has also been accounted for. Equating E_B with the energy at closest approach r_m , gives an equation for the maximum velocity

$$\frac{1}{2}v_m^2 = E_B + \frac{Z}{r_m} \quad (44)$$

assuming Coulomb dominated dynamics we may substitute the equation for a Kepler hyperbola at the closest approach, see Eq. (40),

$$\frac{1}{2}v_m^2 = E_B + \frac{Z^2}{l^2} (1 + e), \quad (45)$$

where for nearly backscattered trajectories $e \approx 1$

$$\frac{1}{2}v_m^2 = E_B + \frac{2Z^2}{l^2}. \quad (46)$$

Now the angular momentum may be written in terms of the maximal velocity

$$l^2 = \frac{4Z^2}{V_m^2 - 2E_B}. \quad (47)$$

The dynamics will depend on the scattering angle, the closer to backscattering the higher the maximum velocity will be. Thus, we can use the scattering angle to help formulate the condition. The scattering angle $\Omega = 2\Psi - \pi$, where Ψ is the asymptote angle, that is the angle between the direction of the incoming asymptotic and closest approach (periapsis) direction, which is given by

$$\cos(\Psi) = -\frac{1}{\sqrt{1 + \frac{2E_B l^2}{Z^2}}}. \quad (48)$$

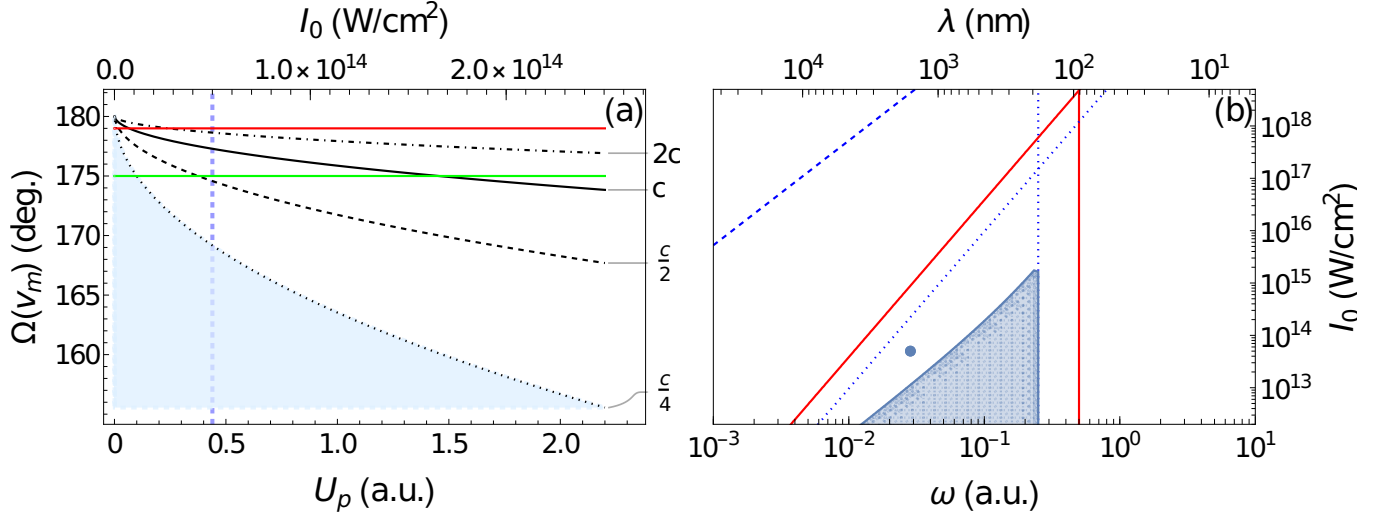


FIG. 7. The limits of a non-relativistic theory for rescattered photoelectrons. (a) the scattering angle, $\Omega(v_m)$, for particular maximum rescattering velocities ($v_m = c/4$, $c/2$, c , and $2c$, given by the dotted, dashed, solid, and dot-dashed black curves, respectively) across a range of intensities, as given by Eq. (49). The shaded region below the curve for $v_m = c/4$ is the region where relativistic effects will not play a role. The wavelength (angular frequency) is fixed to 1600 nm (0.0285 a.u.), the red and green horizontal lines denote a 179° and 175° scattering angle, respectively. The dashed blue vertical line denotes the intensity of $I_0 = 5 \times 10^{13} \text{ W/cm}^2$ ($U_p = 0.44$ a.u.), used in this study. (b) for a range of angular frequencies and intensities, the region where a non-relativistic theory holds for the rescattered photoelectrons is given by the blue shaded region, as given by Eq. (49). This assumes a maximum scattering velocity of $0.25c$ and a maximum scattering angle of 175° . The blue dashed line denotes the typical relativistic condition, $I_0 = 2c^2\omega^2$, while the red solids line denoted the dipole conditions, $\omega = 1/2$ and $I_0 = 8c\omega^3$, outside of which the dipole approximation breaks down. Similarly, the blue dotted lines marked the region where a tunnelling model will hold, $\omega = 1/4$ and $I_0 = 2c\omega^3$, as given in [76]. A blue dot is used to show the parameters used in this study.

Inserting Eq. (47) gives an equation for the scattering angle in terms of the maximal velocity

$$\Omega(v_m) = 2 \arccos \left[-\frac{1}{\sqrt{1 + \frac{8E_B}{v_m^2 - 2E_B}}} \right] - \pi. \quad (49)$$

In FIG. 7(a), contours of Eq. (49) are given for different values of v_m in terms of c . For an increasing laser intensity, the scattering angle (given a fixed maximal velocity) reduces. For the curve, $\Omega(c/4)$, this is used to denote a region (shaded in blue), where relativistic effects may be neglected. As intensity increases, this region reduces so that less of the rescattered wavepacket may be accurately described by a non-relativistic model, as higher velocities will be reached during rescattering. The parameter region in this study (blue dashed line), crosses this boundary for scattering angle greater than 170° , and crossed the $\Omega(2c)$ at around 179° . This is confirmed by FIG. 3, where the long and short orbit 4 trajectories scattered by 179° reach velocities just over $2c$, when neglecting corrections to the kinetic energy. Note that orbit 4b would actually require a strong condition, as it has a return energy of higher than E_B and returns with a $6c$ velocity. However, for these parameters, this solution has low probability.

In FIG. 7(b), we use this condition to construct a modified region (blue shaded region), inside the dipole allowed region, where relativistic effects are not important for

scattering angles $\Omega(0.25c) < 175^\circ$, given a maximal velocity of $v_m = 0.25c$. This reduces the standard dipole allowed region by around a factor of 2, and the blue point representing the parameters used in this study lies outside this region despite being inside the dipole allowed region. Note, the typical relativistic condition (blue dashed line in the upper left of the figure) lies more than 6 order of magnitude in intensity from our modified condition, demonstrating the huge difference that rescattering can make when considering relativistic effects.

VIII. CONCLUSION AND OUTLOOK

Driving atomic and molecular systems with near-infrared light at intensities up to around 10^{14} W/cm^2 was thought to be well described by non-relativistic quantum mechanics [76], besides effects associated with large spin-orbit energy splitting in the cationic system [52]. In this study, we have used the powerful machinery of the path integral-based CQSFA to investigate spin-orbit coupling and other relativistic dynamics in more detail. For the parameter range explored, we find the CQSFA provides an exceptional quantitative agreement with the single-active electron TDSE. However, upon close inspection, we have illustrated that the non-relativistic treatment breaks down for a significant portion of the rescattered

electron wavepacket, at a laser intensity orders of magnitude below that expected.

The origin of this breakdown is that the backscattered electrons probe the core very closely and gain significant kinetic energy. In the non-relativistic treatment, this results in unphysical superluminal velocities of the electron. To remedy this situation, we extended the CQSFA to include all relativistic correction terms from the Briet-Pauli Hamiltonian, including spin-orbit coupling and corrections to the kinetic energy. With this improved model we evaluate the effects of these terms, and find the kinetic energy corrections to be significant for the rescattered part of the electron, while the spin-orbit coupling is massively overestimated if computed without the former. Accordingly, the assessment of dynamical spin-orbit effects by theory not accounting for relativistic kinetic energy corrections (which is common given its inclusion is numerically intensive), need to take care, since such theory would significantly overestimate the spin-orbit interaction effects. In order to inform future work, we provide an expression for where relativistic effects become important, and which lies many orders of magnitude below the typical limit for relativistic effects.

The rescattered region in question is important for application in attosecond physics and chemistry, through imaging processes, such as LIED, where the diffraction pattern of the rescattered electron is used to infer sub-femtosecond nuclear motion in molecules [85, 86]. Clearly, an interpretation of an experimental PMD with a model involving non-relativistic cross-sections would lack the spin-orbit and kinetic energy corrections of focus in this work, and could therefore lead, e.g., to deviations between inferred and actual time-resolved distances. Thus, the models used for LIED should incorporate relativistic scattering cross-sections. Work assessing quantitatively the implications of our findings for this kind of investigation is currently in progress, including adapting the CQSFA for LIED.

The conclusions and perspectives discussed above were obtained from the new theory developments of this work, where an improved non-relativistic quantum trajectory-based CQSFA was used to reach unprecedented agreement with TDSE simulations for PMDs. This agreement allowed us to proceed with a relativistic extension of the CQSFA. The coherent spin formalism and weak-coupling limits allowed such development, including analytical elucidation of the dynamics. The trajectory-based approach benefits from ease of interpretation in terms of possibly interfering quantum paths. Furthermore, the effects of the different coupling terms in the action can easily be isolated. This separation into individual contributions was used here to show the reduction in the spin-orbit action phase by the corrections to the relativistic energy. Such methodologies could also be extended to describe the spin of a residual ion. Furthermore, the coherent spin state formalism opens up the possibility of including other degrees of freedom supported by this description, such as the quantum state of the laser. Which has re-

cently been found to lead to a broad range of significant effects [87–93].

Looking into the future, it would be very interesting to connect this work with recent work on orbital angular momentum in strong-field ionization [94–96] and examine the role of total angular momentum in imaging, as well as the implications for inelastic double ionization processes [97] demonstrating angular momentum entanglement. Another important direction, is to extend the present studies to longer mid-infrared wavelengths, say up to around 3000 nm. This is the wavelength regime of current LIED experiments [85, 86]. The present CQSFA with relativistic corrections is scalable to this wavelength domain, while TDSE-based approaches would be severely challenged by numerical difficulties related to the increase in the required number of total angular momenta, along with relativistic corrections. In this longer wavelength regime, nondipole corrections to the laser-matter interaction would have to be included [76, 98], and this will affect the initial conditions for the trajectories [99], as well as the shape of the PMD and ATI [100, 101].

In addition to the scaling with wavelength, our results also show that the interval of backscattering angles, where relativistic corrections are needed, increases with laser intensity. Mid-infrared intense femtosecond laser pulses are currently becoming more readily accessible, e.g. [102], so we envision increased need for theory incorporating relativistic effects in the future. If the rescattering energy becomes sufficiently large, one could even contemplate laser-induced time-resolved investigations of the structure of the atomic nucleus, with an achievable timescale of less than an attosecond made possible by the very brief electron transit, opening up a new domain on sub-attosecond physics.

ACKNOWLEDGMENTS

ASM acknowledges funding support from the European Union’s Horizon 2020 research and innovation programme under the Marie Skłodowska-Curie grant agreement SSFI No. 887153. LBM acknowledges support from the Danish Council for Independent Research (Grant Nos. 9040-00001B and 1026-00040B).

Appendix A: CQSFA theory

In this Appendix, we discuss some additional approximations that are used in the CQSFA theory.

We use the analytical Kepler expression to extend the trajectories and action asymptotically to infinite time, once the laser pulse is over [68, 103]. The tunnel integral over the binding potential is approximated by the Coulomb-factor [104, 105],

$$\int_{t_s}^{\text{Re}[t_s]} V[\mathbf{r}_s(\tau)] d\tau \approx \left(\frac{4I_p}{|\mathbf{E}(t_s)|} \right)^{\frac{Z}{\sqrt{2}I_p}}. \quad (\text{A1})$$

This approach has two advantages, it automatically regularizes the divergent integral, given by direct evaluation of the integral in Eq. (A1), and avoids branch cuts that arise in this integral, due to taking the square root of the complex-valued position vector over the tunnel exit. As in previous works [55–57], we take the position to be real for real-time propagation, i.e., $\mathbf{r}_s(\text{Re}[t_s]) = \text{Re}[\mathbf{r}_0]$ and keep the momentum fixed during tunnelling, i.e., $\mathbf{p}_s(t) = \mathbf{p}_{0s}$ for $t \in [t_s, \text{Re}[t_s]]$. Here, the tunnel exit is given by

$$\mathbf{r}_0 = \text{Re} \left[\int_{t_s}^{\text{Re}[t_s]} d\tau (\mathbf{p}_{0s} + \mathbf{A}(\tau)) \right]. \quad (\text{A2})$$

Aside from these approximations specifying the initial conditions for the trajectory propagation, all other parts of the action, given by Eq. (4), are computed in full.

Appendix B: Spin-state framework

In order to describe spin in a path-integral framework, we require coherent spin-states [78, 80] (an irreducible representation for $SU(2)$). In its most general form a $SU(2)$ coherent spin state can be written as

$$|z; S\rangle = \frac{e^{zS} |S, m_s = -S\rangle}{(1 + |z|^2)^S}. \quad (\text{B1})$$

For a spin-1/2 ($S = 1/2$) system, dropping all the S 's, this may be written as

$$|z\rangle = \frac{|\downarrow\rangle + z|\uparrow\rangle}{\sqrt{1 + |z|^2}}, \quad (\text{B2})$$

where we use $|\uparrow\rangle$ ($|\downarrow\rangle$) to denote $m_s = \frac{1}{2}$ ($m_s = -\frac{1}{2}$). A vital step when deriving a path integral representation of a propagator is insertion of the resolution of the identity in time sliced amplitudes. For coherent spin-states the resolution of the identity may be written as

$$I_S = \int d\mu_S(z) |z; S\rangle \langle z; S|, \quad d\mu_S(z) = \frac{2S+1}{\pi} \frac{d^2 Z}{(1 + |z|^2)^2} \quad (\text{B3})$$

The coherent spin states map spin states to the complex plane, see FIG. 4. Some key values are $|z \rightarrow 0\rangle = |\downarrow\rangle$, $|z \rightarrow \infty\rangle = |\uparrow\rangle$, $|z \rightarrow 1\rangle = \frac{1}{2}(|\uparrow\rangle + |\downarrow\rangle)$ and $|z \rightarrow -1\rangle = \frac{1}{2}(|\uparrow\rangle - |\downarrow\rangle)$.

It is useful to apply this formalism to building eigenstates of the field-free system, i.e. $\hat{H}_{0,\text{SO}} = \hat{H}_0 + \hat{H}_{\text{SO}}$. Consider an initial state with quantum numbers j and m_j , built using the standard angular momentum addition rules, e.g., see Ref. [4].

$$|\Phi_{jm_j}\rangle = \sum_{m, m_s} \langle l, S; m, m_s | l, S; j, m_j \rangle \otimes |\psi_{lm}\rangle |S; m_s\rangle, \quad (\text{B4})$$

where $|\psi_{lm}\rangle$ is an eigenstate of the square of the orbital angular momentum and its projection on the quantization axis, \hat{L}_z . For $S = 1/2$ we can write $|\Phi_{jm_j}\rangle$ in terms of the coherent spin state

$$|\Phi_{jm_j}\rangle = \sum_m f_{lm}^{jm_j} |z_{lm}^{jm_j}\rangle \otimes |\psi_{lm}\rangle \quad (\text{B5})$$

with $f_{lm}^{jm_j} = C_{lm, \frac{1}{2} - \frac{1}{2}}^{jm_j} \sqrt{1 + |z_{lm}^{jm_j}|^2}$, $z_{lm}^{jm_j} = C_{lm, \frac{1}{2} - \frac{1}{2}}^{jm_j} / C_{lm, \frac{1}{2} - \frac{1}{2}}^{jm_j}$ and $C_{lm, S m_s}^{jm_j} = \langle l, S; m, m_s | l, S; j, m_j \rangle$, Eq. (B5) is the same as Eq. (17) in the main text. Thus, the initial spin state is represented through a sum of coherent spin states.

Appendix C: Path-Integral with Spin

In this section we provide a more in-depth derivation of the final path-integral expression, we present the weak approximation in more detail, see Eq. (27) in the main manuscript, and we present a derivation of a modified saddle-point approximation that could be used for cases of strong spin-orbit coupling. We did not use the modified saddle-point approximation in the main manuscript because it is significantly more complex than the weak coupling approximation, which is valid for the case of hydrogen. Employing the coherent state formalism, introduced above, we are in a position to utilize the path-integral formalism for a particle with spin [78, 80–82], and can evaluate the kernel $\mathcal{K}_m(\mathbf{p}, z)$ (defined in Eq. (22))

$$\mathcal{K}_m(\mathbf{p}, z) = \int_{\mathbf{r}_0} \frac{D'\mathbf{r}}{(2\pi)^3} \int_{\mathbf{p}}^{p_f} D'\mathbf{p} \int_{z_{lm}^{jm_j}}^z D\mu(z) d_m(\mathbf{p}_0, t') e^{i\mathcal{A}[\mathbf{r}, \mathbf{p}, z, t']}, \quad (\text{C1})$$

where

$$\mathcal{A}[\mathbf{r}, \mathbf{p}, z, t'] = - \int_{t'}^\infty d\tau \left[\dot{\mathbf{p}} \cdot \mathbf{r} + iS \frac{z\dot{z}^* - z^*\dot{z}}{1 + |z|^2} + H(\mathbf{r}, \mathbf{p} + \mathbf{A}(\tau), z, t') \right] \quad (\text{C2})$$

and

$$H(\mathbf{r}, \mathbf{p}, z, \tau) = K(\mathbf{p}) + U(\mathbf{r}) + \mathbf{C}_{\text{SO}}(\mathbf{r}, \mathbf{p}) \cdot \mathbf{n}(z). \quad (\text{C3})$$

Here, $\mathbf{n}(z)$ is a semiclassical representation of \hat{S} , such that $\mathbf{n}(z) = (n_1, n_2, n_3)$, $n_1 + in_2 = 2z^*/(1 + |z|^2)$ and $n_3 = -(1 - |z|^2)/(1 + |z|^2)$.

1. Weak-coupling limit

The kernel, given by Eq. (22) may be solving using the saddle-point approximation, however, a simpler solution

is possible via the so-called weak approximation. The first step is to use the fact that the functional integral over z may be solved analytically. Rewriting Eq. (C1) as

$$\mathcal{K}_m(\mathbf{p}, z) = \int_{\mathbf{r}_0} \frac{\mathcal{D}'\mathbf{r}}{(2\pi)^3} \int_{\mathbf{p}_f} \mathcal{D}'\mathbf{p} \mathcal{M}_{\text{SO}}^m(\mathbf{r}, \mathbf{p}, z, t') d_m(\mathbf{p}_0, t') e^{i\mathcal{A}_{0,I}[\mathbf{r}, \mathbf{p}, t']}, \quad (\text{C4})$$

where all spin and spin-orbit term are collected in

$$\mathcal{M}_{\text{SO}}^m(\mathbf{r}, \mathbf{p}, z, t') = \int_{z_{lm}^{jm_j}}^z \mathcal{D}\mu(z) e^{i\mathcal{A}_{\text{SO}}[\mathbf{r}, \mathbf{p}, z, t']}. \quad (\text{C5})$$

Here,

$$\mathcal{A}_{0,I}[\mathbf{r}, \mathbf{p}, t'] = - \int_{t'}^{\infty} d\tau [\dot{\mathbf{p}} \cdot \mathbf{r} + H_{0,I}(\mathbf{r}, \mathbf{p} + \mathbf{A}(\tau), \tau)] \quad (\text{C6})$$

and

$$\mathcal{A}_{\text{SO}}[\mathbf{r}, \mathbf{p}, z, t'] = - \int_{t'}^{\infty} d\tau \left[iS \frac{z\dot{z}^* - z^*\dot{z}}{1 + |z|^2} + H_{\text{SO}}(\mathbf{r}, \mathbf{p} + \mathbf{A}(\tau), z) \right], \quad (\text{C7})$$

where $H_{0,I}(\mathbf{r}, \mathbf{p}, \tau) = K(\mathbf{p}) + U(\mathbf{r})$ and $H_{\text{SO}}(\mathbf{r}, \mathbf{p}, z) = \mathbf{C}_{\text{SO}}(\mathbf{r}, \mathbf{p}) \cdot \mathbf{n}(z)$. It is possible to solve Eq. (C5) as [81]

$$\mathcal{M}_{\text{SO}}^m(\mathbf{r}, \mathbf{p}, z, t') = \frac{a^*(t) - b^*(t)z_{lm}^{jm_j*} + b(t)z + a(t)z^*z_{lm}^{jm_j}}{\sqrt{1 + |z|^2} \sqrt{1 + |z_{lm}^{jm_j}|^2}}, \quad (\text{C8})$$

where $a(t)$ and $b(t)$ may be obtained by solving the following ordinary differential equation (ODE) [81]

$$\begin{aligned} \dot{a} &= -\frac{i}{2c^2r} \frac{dV}{dr} (L_z(t)a - (L_x(t) - iL_y(t))b^*), \\ \dot{b} &= -\frac{i}{2c^2r} \frac{dV}{dr} (L_z(t)b + (L_x(t) - iL_y(t))a^*) \end{aligned} \quad (\text{C9})$$

with $a(0) = 1$, $b(0) = 0$ and $\mathbf{L}(t) = \mathbf{r}(t) \times (\mathbf{p}(t) + \mathbf{A}(t))$.

Now that we have a solution for $\mathcal{M}_{\text{SO}}^m(\mathbf{r}, \mathbf{p}, z, t')$, we may solve the remaining path integral with the saddle-point approximation, as in the spin-less version. Here, we assume that $\mathcal{M}_{\text{SO}}^m(\mathbf{r}, \mathbf{p}, z, t')$ is a slowly varying function like $d_m(p, t')$ and treat it as a prefactor in the semi-classical approximation. This is a weak-coupling approximation, such as employed in Ref. [81], assuming that there is an effect of the trajectory motion on the spin but not vice versa, and will be valid if the spin-orbit action (Eq. (37) in main text) is appreciably lower than

the rest of the action. Thus, the final expression for the transition amplitude is given by

$$M(\mathbf{p}, z) = \quad (\text{C10})$$

$$= -i \sum_{m,s} C_m(\mathbf{r}_s, \mathbf{p}_s, t_s) \mathcal{M}_{\text{SO}}^m(\mathbf{r}_s, \mathbf{p}_s, z_s, t_s) e^{iS[\mathbf{r}_s, \mathbf{p}_s, t_s]} \quad (\text{C11})$$

with

$$C(\mathbf{r}_s, \mathbf{p}_s, t_s) = \sqrt{\frac{2\pi i}{\partial^2 S / \partial t'^2}} \frac{e^{-i\pi\nu/2}}{\sqrt{|J|}} d_m(\mathbf{p}_{0s}, t_s), \quad (\text{C12})$$

which are the expressions stated in the main text.

2. Modified Saddle-Point Approximation

In this section, we present an alternative to the weak approximation that was used in the main text to formulate the CQSFA transition amplitude that included spin-orbit coupling Eq. (C11). The weak approximation requires that the action for spin-orbit coupling is significantly less than the remaining action. However, instead it is possible to apply the saddle-point approximation to the full path integral, which allows its use for systems with higher spin-orbit coupling, e.g., for larger atoms. This has been called the extended phase space formulation [81], as it treats the real and imaginary parts of the coherent spin state coefficient like an extra component of position and momentum. Although this formalism has the potential to be quite powerful and descriptive, there were a number of reasons that we did not use it in the main text. Firstly, it breaks the cylindrical symmetry of the equations of motion, this means simplifications that exploit this can not be used, making the calculation more numerically intensive. Secondly, the computation of the fluctuation factor, Eq. (C14) is non-trivial and goes beyond the scope of this work. Finally, for strong-field ionization of hydrogen, the weak approximation remains valid and can be very simply expressed as a prefactor term. Hence, to derive the modified saddle-point approximation, we evaluate Eq. (23) directly via the saddle point approximation leading to

$$M(\mathbf{p}, z; \Phi_{jm_j}) = \sum_{m,s} \sqrt{\frac{2\pi i}{\partial^2 S / \partial t'^2}} \mathcal{F} d_m(\tilde{\mathbf{p}}_{0s}, t_s) e^{iS[\mathbf{r}_s, \mathbf{p}_s, z_s, t_s]}. \quad (\text{C13})$$

This expression is very similar to that in Eq. (C5), except here the saddle-points are different, and the fluctuation factor \mathcal{F} can be determined by

$$\mathcal{F} = \int \mathcal{D}[\boldsymbol{\eta}] \exp(i\mathcal{A}^{(2)}(\boldsymbol{\eta})), \quad (\text{C14})$$

where $\boldsymbol{\eta} = (\delta\mathbf{r}, \delta v, \delta\mathbf{p}, \delta u)$ (given $z = u - iv$), which is known as the extended phase-space vector of small variations [78]. The second variation of the action is given

by

$$\mathcal{A}^{(2)}(\boldsymbol{\eta}) = \frac{1}{2} \left(\boldsymbol{\eta} \cdot \Gamma \dot{\boldsymbol{\eta}} - \boldsymbol{\eta} \cdot \frac{\partial^2 H}{\partial \boldsymbol{\eta} \partial \boldsymbol{\eta}} \boldsymbol{\eta} \right), \quad (\text{C15})$$

where $\Gamma = \begin{pmatrix} 0 & \mathbb{1}_4 \\ -\mathbb{1}_4 & 0 \end{pmatrix}$ (known as the 8-dimensional unit symplectic matrix), with $\mathbb{1}_4$ being the 4-dimensional identity matrix. The saddle-point equations are given by

$$\dot{\mathbf{r}} = \frac{\partial H}{\partial \mathbf{p}} = \mathbf{p} + \mathbf{A}(\tau) + \mathbf{C}_{SO}(\mathbf{r}, \mathbf{n}(z)) \quad (\text{C16})$$

$$\dot{\mathbf{p}} = -\frac{\partial H}{\partial \mathbf{r}} = -\nabla U(\mathbf{r}) - \frac{1}{|\mathbf{r}|} \mathbf{C}_{SO}(|\mathbf{r}| \mathbf{n}(z), \mathbf{p}) \quad (\text{C17})$$

while the equations for \dot{z} use $z = u - iu$

$$\dot{u} = (1 + |z|^2)^2 \frac{1}{2} \frac{\partial H}{\partial u} = \mathbf{C}_{SO}(\mathbf{r}, \mathbf{p}) \cdot \begin{pmatrix} 1 - u^2 + v^2 \\ -2uv \\ 2u \end{pmatrix} \quad (\text{C18})$$

$$\dot{v} = (1 + |z|^2)^2 \frac{1}{2} \frac{\partial H}{\partial v} = \mathbf{C}_{SO}(\mathbf{r}, \mathbf{p}) \cdot \begin{pmatrix} -2uv \\ 1 + u^2 - v^2 \\ 2v \end{pmatrix}, \quad (\text{C19})$$

which provides equations of motion for the spin. This is an alternative to what was used in the main text, where the spin-orbit coupling did not affect the equations of motion for the electron trajectories. Now the position, momentum, and spin are determined by coupled equations. This provides a very flexible formalism to describing spin through a path integral and connect it to semiclassical equations of motion, which can provide crucial insight into the dynamics. This could also be applied to describe the spin of the residual ion, where for a multielectron description a higher dimensional representation of the coherent spin state can be used. Such a description is not restricted to spin, and a similar formalism could potentially be used to incorporate the quantum state of the light field via a coherent state path integral.

Appendix D: Spin Averaging

We may use the coherent spin state formalism to average incoherently over initial spin orientations, for hydrogen, we use the spin state $|\Phi_{1/2 \pm 1/2}\rangle = |z_{00}^{1/2 \pm 1/2}\rangle |\psi_{00}(t')\rangle$, where either $z^{1/2 \pm 1/2} \rightarrow 0$ (spin down) or $z^{1/2 \pm 1/2} \rightarrow \infty$ (spin up). The state $|\psi_{00}(t')\rangle$ indicates that the spatial part is initially in a s state with $l = m = 0$. Spatial rotations to the initial state means that all possible value of initial z_{00} will be covered. We can show this explicitly by integrating over the Euler angles (see Eq. (29) of the main text)

$$\mathcal{P}_{\uparrow}(\mathbf{p}) = \frac{1}{8\pi^2} \int_0^{2\pi} d\alpha \int_0^\pi d\beta \int_0^{2\pi} d\gamma \sin(\beta) \mathcal{P}_{\uparrow}(\mathbf{p}; \mathcal{R}_{\alpha\beta\gamma} |\uparrow\rangle). \quad (\text{D1})$$

Parameterizing the rotating as $\mathcal{R}_{\alpha\beta\gamma} = \exp(-i\alpha\sigma_z/2) \exp(-i\beta\sigma_y/2) \exp(-i\gamma\sigma_z/2)$, we may write the rotation of the spin up state as

$$\mathcal{R}_{\alpha\beta\gamma} |\uparrow\rangle = e^{i\gamma/2} (e^{-i\alpha/2} \cos(\beta/2) |\uparrow\rangle + e^{i\alpha/2} \sin(\beta/2) |\downarrow\rangle). \quad (\text{D2})$$

This may be written in terms of coherent spin states

$$\mathcal{R}_{\alpha\beta\gamma} |\uparrow\rangle = e^{i\alpha/2 - i\gamma/2} |e^{-i\alpha} \cot(\beta/2)\rangle. \quad (\text{D3})$$

We may drop the phasor prefactors as these will not contribute in the incoherent average, which may be written as

$$\mathcal{P}_{\uparrow}(\mathbf{p}) = \frac{1}{8\pi^2} \int_0^{2\pi} d\alpha \int_0^\pi d\beta \int_0^{2\pi} d\gamma \sin(\beta) \mathcal{P}_{\uparrow}(\mathbf{p}; |e^{-i\alpha} \cot(\beta/2)\rangle) \quad (\text{D4})$$

$$= \frac{1}{4\pi} \int_0^{2\pi} d\alpha \int_0^\pi d\beta \sin(\beta) \mathcal{P}_{\uparrow}(\mathbf{p}; |e^{-i\alpha} \cot(\beta/2)\rangle). \quad (\text{D5})$$

As there is no γ dependence we could do the γ integral directly. To continue, we make the variable transformation $\phi_0 = -\alpha$ and $u_0 = \cot(\beta/2)$. The u_0 integration metric can be written as $du_0 = -\frac{d\beta}{2\sin(\beta/2)^2}$, which means that $d\beta \sin(\beta) = -\frac{4u}{(1+u^2)^2}$. This means the averaged probability may be written as

$$\mathcal{P}_{\uparrow}(\mathbf{p}) = \frac{1}{\pi} \int_0^{2\pi} d\phi_0 \int_0^\infty u du \frac{1}{(1+u^2)^2} \mathcal{P}_{\uparrow}(\mathbf{p}; |u_0 e^{i\phi_0}\rangle). \quad (\text{D6})$$

$$= \frac{2}{\pi} \int_{\mathbb{C}} d^2 z_{00} \frac{1}{(1+|z_{00}|^2)^2} \mathcal{P}_{\uparrow}(\mathbf{p}; |z_{00}\rangle), \quad (\text{D7})$$

where we have let $z_{00} = u_0 e^{i\phi_0}$ with $dz_{00}^2 = dz_{00} \wedge dz_{00}^* = 2i u du_0 \wedge d\phi_0$ leading to the integral over the coherent spin states.

Now we can compute the spin average using Eq. (D7). We may write the probably given an initial z_{00} and final spin up using the weak-coupling formalism, but without actually applying any approximation, so it is still exact. The probability is given by

$$\mathcal{P}_{\uparrow}(\mathbf{p}; z_0) = \left| \int_{-\infty}^{\infty} dt' \int \mathcal{D}\mathbf{r} \int \frac{\mathcal{D}'\mathbf{p}}{(2\pi)^3} \mathcal{M}_{SO}^{\uparrow}(\mathbf{r}, \mathbf{p}, t'; z_0) d(\mathbf{p}_0, t') e^{iS_0[\mathbf{r}, \mathbf{p}, t']} \right|^2. \quad (\text{D8})$$

Only the term $\mathcal{M}_{SO}^{\uparrow}(\mathbf{r}, \mathbf{p}, t', z_0)$ contains dependence on z_0 , from Eq. (C8) this term may be written as

$$\mathcal{M}_{SO}^{\uparrow}(\mathbf{r}, \mathbf{p}, t', z_0) = \frac{b + a z_0}{\sqrt{1 + |z_0|^2}}, \quad (\text{D9})$$

similarly for $\mathcal{M}_{\text{SO}}^\downarrow$ we have

$$\mathcal{M}_{\text{SO}}^\downarrow(\mathbf{r}, \mathbf{p}, t', z_0) = \frac{a - b^* z_0^*}{\sqrt{1 + |z_0|^2}}. \quad (\text{D10})$$

Here we took $z_f \rightarrow \infty$ for spin up and $z_f \rightarrow 0$ for spin down. We proceed by writing in more compact notation, we collect t' , \mathbf{r} and \mathbf{p} into x and set $\mathcal{M}_{0,I}(x) = d(x)e^{iS_{0,I}(x)}$. Now the spin-averaged probability is

$$\mathcal{P}_\uparrow(\mathbf{p}, z_0) = \frac{2}{\pi} \int_{\mathbb{C}} d^2 z_0 \frac{1}{(1 + |z_0|^2)^2} \left| \int \mathcal{D}x \frac{b(x) + a(x)z_0}{\sqrt{1 + |z_0|^2}} \mathcal{M}_{0,I}(x) \right|^2 \quad (\text{D11})$$

$$= \frac{2}{\pi} \int \mathcal{D}x \int \mathcal{D}x' \mathcal{M}_{0,I}(x) \mathcal{M}_{0,I}^*(x') \int_{\mathbb{C}} d^2 z_0 \frac{1}{(1 + |z_0|^2)^2} \left(\frac{b(x) + a(x)z_0}{\sqrt{1 + |z_0|^2}} \right) \left(\frac{b^*(x') + a^*(x')z_0^*}{\sqrt{1 + |z_0|^2}} \right) \quad (\text{D12})$$

$$= \frac{2}{\pi} \int \mathcal{D}x \int \mathcal{D}x' \mathcal{M}_{0,I}(x) \mathcal{M}_{0,I}^*(x') \underbrace{\int_{\mathbb{C}} d^2 z_0 \frac{(b(x) + a(x)z_0)(b^*(x') + a^*(x')z_0^*)}{(1 + |z_0|^2)^3}}_I \quad (\text{D13})$$

Here we pull out the integral over spin states and do this separately

$$I = \int_{\mathbb{C}} d^2 z_0 \frac{(b(x) + a(x)z_0)(b^*(x') + a^*(x')z_0^*)}{(1 + |z_0|^2)^3} \quad (\text{D14})$$

$$= \int_{\mathbb{C}} d^2 z_0 \frac{b(x)b^*(x') + b(x)a^*(x')z_0^* + a(x)b^*(x')z_0 + a(x)a^*(x')|z_0|^2}{(1 + |z_0|^2)^3} \quad (\text{D15})$$

$$= -2 \int_0^\infty du_0 \int_0^{2\pi} d\phi_0 \frac{b(x)b^*(x') + b(x)a^*(x')u_0 e^{-i\phi_0} + a(x)b^*(x')u_0 e^{i\phi_0} + a(x)a^*(x')u_0^2}{(1 + u_0^2)^3} \quad (\text{D16})$$

$$= - \int_0^\infty u_0 du_0 \frac{4\pi(b(x)b^*(x') + a(x)a^*(x')u_0^2)}{(1 + u_0^2)^3} \quad (\text{D17})$$

$$= \pi(b(x)b^*(x') + a(x)a^*(x')). \quad (\text{D18})$$

Inserting the integral back into Eq. (D13) gives

$$\mathcal{P}_\uparrow(\mathbf{p}) = \int \mathcal{D}x \int \mathcal{D}x' \mathcal{M}_{0,I}(x) \mathcal{M}_{0,I}^*(x') (b(x)b^*(x') + a(x)a^*(x')) \quad (\text{D19})$$

$$= \left| \int \mathcal{D}x a(x) \mathcal{M}_{0,I}(x) \right|^2 + \left| \int \mathcal{D}x b(x) \mathcal{M}_{0,I}(x) \right|^2 \quad (\text{D20})$$

$$= \mathcal{P}_{\uparrow;\uparrow}(\mathbf{p}) + \mathcal{P}_{\uparrow;\downarrow}(\mathbf{p}).$$

Given that, $\mathcal{M}_{\text{SO}}^\uparrow(\mathbf{r}, \mathbf{p}, t', z_0) \rightarrow a$ as $z_0 \rightarrow \infty$ and $\mathcal{M}_{\text{SO}}^\uparrow(\mathbf{r}, \mathbf{p}, t', z_0) \rightarrow b$ as $z_0 \rightarrow 0$. By the same logic $\mathcal{P}_{\downarrow}(\mathbf{p}) = \mathcal{P}_{\downarrow;\uparrow}(\mathbf{p}) + \mathcal{P}_{\downarrow;\downarrow}(\mathbf{p})$.

Appendix E: Characterizing the dynamical spin coefficients $a(t)$ and $b(t)$

Given that we restrict dynamics to the zy -plane and the orbital angular momentum consequently is in the x -direction, the ODE for $a(t)$ and $b(t)$ Eq. (C9) may be

written as

$$\begin{aligned} \dot{a}(t) &= -\frac{i}{2c^2 r} \frac{dV}{dr} L_x(t) b^*(t), \\ \dot{b}(t) &= -\frac{i}{2c^2 r} \frac{dV}{dr} L_x(t) a^*(t). \end{aligned} \quad (\text{E1})$$

By writing $a(t)$ and $b(t)$ explicitly in terms of real and imaginary parts, this set of ODEs may be written as a 4-vector equation $\dot{\mathbf{x}}(t) = H_{\text{SO}}(t) \underline{\underline{\eta}} \mathbf{x}(t)$ with $\mathbf{x}(t) = (\text{Re}[a(t)], \text{Im}[a(t)], \text{Re}[b(t)], \text{Im}[b(t)])$ and

$$\underline{\underline{\eta}} = \begin{pmatrix} 0 & 0 & 0 & 1 \\ 0 & 0 & -1 & 0 \\ 0 & 1 & 0 & 0 \\ -1 & 0 & 0 & 0 \end{pmatrix}, \quad (\text{E2})$$

$$H_{\text{SO}}(t) = \frac{1}{2cr^2} \frac{dV}{dr} L_x(t) \quad (\text{E3})$$

Thus $a(t)$ and $b(t)$ may be solved, see [106], as

$$\begin{aligned} a(t) &= \mathbf{x}_a \cdot \left[\exp \left(\int dt H_{\text{SO}}(t) \underline{\underline{\eta}} \right) \mathbf{x}_0 \right] \\ b(t) &= \mathbf{x}_b \cdot \left[\exp \left(\int dt H_{\text{SO}}(t) \underline{\underline{\eta}} \right) \mathbf{x}_0 \right], \end{aligned} \quad (\text{E4})$$

where the dot product with $\mathbf{x}_a(t) = (1, i, 0, 0)$ selects the real and imaginary components of $a(t)$ and $\mathbf{x}_b = (0, 0, 1, i)$ selects the real and imaginary components of $b(t)$. The initial condition is $a(0) = 1$, which means $\mathbf{x}_0 = (1, 0, 0, 0)$, this leads to the solutions

$$\begin{aligned} a(t) &= \cos(S_{\text{SO}}(t)), \\ b(t) &= -i \sin(S_{\text{SO}}(t)), \end{aligned} \quad (\text{E5})$$

which are the solutions used in the discussion in Sec. V.B.

Appendix F: Relativistic Force Corrections

Here we consider the equations of motion with relativistic correction to the kinetic energy to better understand why the core gets less strongly probed with than without these corrections. Hamilton's equations of motion are given by

$$\dot{\mathbf{r}} = \nabla_{\mathbf{p}} K(\mathbf{p}), \quad \dot{\mathbf{p}} = -\nabla_{\mathbf{r}} U(\mathbf{r}). \quad (\text{F1})$$

Considering only the relativistic corrections to kinetic energy we have $K(\mathbf{p}) = \frac{1}{2}\mathbf{p}^2 - \frac{1}{8c^2}\mathbf{p}^4$, with $\nabla_{\mathbf{p}} K(\mathbf{p}) = (1 - \frac{1}{2c^2}\mathbf{p}^2)\mathbf{p}$. Taking the derivative of $\dot{\mathbf{r}}$ with respect to time and writing $\mathbf{F} = -\nabla_{\mathbf{r}} U$, we obtain a Newtonian style force equation

$$\ddot{\mathbf{r}} = (1 - \frac{1}{2c^2}\underline{\underline{M}})\mathbf{F}, \quad (\text{F2})$$

where $\underline{\underline{M}}$ is a matrix given by $\underline{\underline{M}} = \mathbf{1}_3\mathbf{p}^2 + 2\mathbf{p} \otimes \mathbf{p}$. Thus, the matrix $\underline{\underline{M}}$ determines by how much the force is effectively reduced by from the classical case. For example, in the case the electron is heading directly to the residual ion, $\mathbf{p} = (0, 0, v)$ and $\mathbf{F} = (0, 0, F)$

$$\underline{\underline{M}} = \begin{pmatrix} v^2 & 0 & 0 \\ 0 & v^2 & 0 \\ 0 & 0 & 3v^2 \end{pmatrix} \quad (\text{F3})$$

leading to the equation

$$\ddot{z} = (1 - \frac{3v^2}{2c^2})F, \quad (\text{F4})$$

While, in the case that the electron is travelling perpendicular to force due to the residual ion, $\mathbf{p} = (0, v, 0)$ and $\mathbf{F} = (0, 0, F)$ $\underline{\underline{M}}$ is the same as before, but a different component is non-zero leading to the equation

$$\ddot{z} = (1 - \frac{v^2}{2c^2})F. \quad (\text{F5})$$

This effective reduction of the central force will lead to the orbital radius increasing, and thus the core is probed less strongly. These aspects are discussed in Sec. VI of the main text.

-
- [1] G. E. Uhlenbeck and S. Goudsmit, Ersetzung der Hypothese vom unmechanischen Zwang durch eine Forderung bezüglich des inneren Verhaltens jedes einzelnen Elektrons, *Die Naturwissenschaften* **13**, 953 (1925).
 - [2] P. Zeeman, The Effect of Magnetisation on the Nature of Light Emitted by a Substance, *Nature* **55**, 347 (1897).
 - [3] N. F. Mott, Scattering of Electrons by Gold, *Nature* **124**, 986 (1929).
 - [4] I. Barth and O. Smirnova, Spin-polarized electrons produced by strong-field ionization, *Physical Review A* **88**, 013401 (2013).
 - [5] A. Hartung, F. Morales, M. Kunitski, K. Henrichs, A. Laucke, M. Richter, T. Jahnke, A. Kalinin, M. Schöffler, L. P. H. Schmidt, M. Ivanov, O. Smirnova, and R. Dörner, Electron spin polarization in strong-field ionization of xenon atoms, *Nature Photonics* **10**, 526 (2016).
 - [6] P. B. Corkum, Plasma perspective on strong field multiphoton ionization, *Phys. Rev. Lett.* **71**, 1994 (1993).
 - [7] F. Krausz and M. Ivanov, Attosecond physics, *Reviews of Modern Physics* **81**, 163 (2009).
 - [8] P. Salieres, A. L'Huillier, P. Antoine, and M. Lewenstein, Study of The Spatial and Temporal Coherence of High-Order Harmonics, in *Advances In Atomic, Molecular, and Optical Physics*, Vol. 41, edited by B. Bederson and H. Walther (Academic Press, 1999) pp. 83–142.
 - [9] M. Lewenstein and A. L'Huillier, Principles of Single Atom Physics: High-Order Harmonic Generation, Above-Threshold Ionization and Non-Sequential Ionization, in *Strong Field Laser Physics*, Springer Series in Optical Sciences, edited by T. Brabec (Springer, New York, NY, 2009) pp. 147–183.
 - [10] M. F. Ciappina, J. A. Pérez-Hernández, A. S. Landsman, W. A. Okell, S. Zherebtsov, B. Förg, J. Schötz, L. Seiffert, T. Fennel, T. Shaaran, T. Zimmermann, A. Chacón, R. Guichard, A. Zaïr, J. W. G. Tisch, J. P. Marangos, T. Witting, A. Braun, S. A. Maier, L. Roso, M. Krüger, P. Hommelhoff, M. F. Kling, F. Krausz, and M. Lewenstein, Attosecond physics at the nanoscale, *Reports on Progress in Physics* **80**, 054401 (2017).
 - [11] P. M. Paul, E. S. Toma, P. Breger, G. Mullot, F. Augé, Ph. Balcou, H. G. Muller, and P. Agostini, Observation of a Train of Attosecond Pulses from High Harmonic Generation, *Science* **292**, 1689 (2001).
 - [12] M. Hentschel, R. Kienberger, C. Spielmann, G. A. Reider, N. Milosevic, T. Brabec, P. Corkum, U. Heinzmann, M. Drescher, and F. Krausz, Attosecond metrology, *Nature* **414**, 509 (2001).
 - [13] M. Lewenstein, Ph. Balcou, M. Yu. Ivanov, A. L'Huillier, and P. B. Corkum, Theory of high-harmonic generation by low-frequency laser fields, *Physical Review A* **49**, 2117 (1994).

- [14] P. Agostini, F. Fabre, G. Mainfray, G. Petite, and N. K. Rahman, Free-Free Transitions Following Six-Photon Ionization of Xenon Atoms, *Physical Review Letters* **42**, 1127 (1979).
- [15] G. G. Paulus, W. Becker, W. Nicklich, and H. Walther, Rescattering effects in above-threshold ionization : A classical model, *Journal of Physics B: Atomic and Molecular Physics* **27**, L703 (1994).
- [16] M. Lewenstein, K. C. Kulander, K. J. Schafer, and P. H. Bucksbaum, Rings in above-threshold ionization: A quasiclassical analysis, *Phys. Rev. A* **51**, 1495 (1995).
- [17] T. Zuo, A. D. Bandrauk, and P. B. Corkum, Laser-induced electron diffraction: A new tool for probing ultrafast molecular dynamics, *Chemical Physics Letters* **259**, 313 (1996).
- [18] H. Niikura, F. Légaré, R. Hasbani, A. D. Bandrauk, M. Y. Ivanov, D. M. Villeneuve, and P. B. Corkum, Sub-laser-cycle electron pulses for probing molecular dynamics, *Nature* **417**, 917 (2002).
- [19] K. Amini and J. Biegert, Chapter Three - Ultrafast electron diffraction imaging of gas-phase molecules, in *Advances In Atomic, Molecular, and Optical Physics*, Vol. 69, edited by L. F. Dimauuro, H. Perrin, and S. F. Yelin (Academic Press, 2020) pp. 163–231.
- [20] A. Sanchez, K. Amini, S.-J. Wang, T. Steinle, B. Belsa, J. Danek, A. T. Le, X. Liu, R. Moshhammer, T. Pfeifer, M. Richter, J. Ullrich, S. Gräfe, C. D. Lin, and J. Biegert, Molecular structure retrieval directly from laboratory-frame photoelectron spectra in laser-induced electron diffraction, *Nature Communications* **12**, 1520 (2021).
- [21] U. D. Giovannini, J. Küpper, and A. Trabattoni, New perspectives in time-resolved laser-induced electron diffraction, *Journal of Physics B: Atomic, Molecular and Optical Physics* **56**, 054002 (2023).
- [22] Y. Huismans, A. Rouzée, A. Gijsbertsen, J. H. Jungmann, A. S. Smolkowska, P. S. W. M. Logman, F. Lépine, C. Cauchy, S. Zamith, T. Marchenko, J. M. Bakker, G. Berden, B. Redlich, A. F. G. van der Meer, H. G. Muller, W. Vermin, K. J. Schafer, M. Spanner, M. Yu. Ivanov, O. Smirnova, D. Bauer, S. V. Popruzhenko, and M. J. J. Vrakking, Time-Resolved Holography with Photoelectrons, *Science* **331**, 61 (2011).
- [23] D. D. Hickstein, P. Ranitovic, S. Witte, X. M. Tong, Y. Huismans, P. Arpin, X. Zhou, K. E. Keister, C. W. Hogle, B. Zhang, C. Ding, P. Johnsson, N. Toshima, M. J. J. Vrakking, M. M. Murnane, and H. C. Kapteyn, Direct visualization of laser-driven electron multiple scattering and tunneling distance in strong-field ionization, *Phys. Rev. Lett.* **109**, 073004 (2012).
- [24] C. Figueira de Morisson Faria and A. S. Maxwell, It is all about phases: Ultrafast holographic photoelectron imaging, *Reports on Progress in Physics* **83**, 034401 (2020).
- [25] H. R. Reiss, Complete Keldysh theory and its limiting cases, *Physical Review A* **42**, 1476 (1990).
- [26] H. R. Reiss, Relativistic strong-field photoionization, *Journal of the Optical Society of America B* **7**, 574 (1990).
- [27] M. Protopapas, C. H. Keitel, and P. L. Knight, Atomic physics with super-high intensity lasers, *Reports on Progress in Physics* **60**, 389 (1997).
- [28] M. W. Walser, D. J. Urbach, K. Z. Hatsagortsyan, S. X. Hu, and C. H. Keitel, Spin and radiation in intense laser fields, *Physical Review A* **65**, 043410 (2002).
- [29] M. Klaiber, E. Yakaboylu, and K. Z. Hatsagortsyan, Above-threshold ionization with highly charged ions in superstrong laser fields. I. Coulomb-corrected strong-field approximation, *Physical Review A* **87**, 023417 (2013).
- [30] M. Klaiber, E. Yakaboylu, and K. Z. Hatsagortsyan, Above-threshold ionization with highly charged ions in superstrong laser fields. II. Relativistic Coulomb-corrected strong-field approximation, *Physical Review A* **87**, 023418 (2013).
- [31] M. Klaiber, E. Yakaboylu, C. Müller, H. Bauke, G. G. Paulus, and K. Z. Hatsagortsyan, Spin dynamics in relativistic ionization with highly charged ions in superstrong laser fields, *Journal of Physics B: Atomic, Molecular and Optical Physics* **47**, 065603 (2014).
- [32] M. Klaiber, K. Z. Hatsagortsyan, J. Wu, S. S. Luo, P. Grugan, and B. C. Walker, Limits of Strong Field Rescattering in the Relativistic Regime, *Physical Review Letters* **118**, 093001 (2017).
- [33] M. Klaiber, J. Daněk, E. Yakaboylu, K. Z. Hatsagortsyan, and C. H. Keitel, Strong-field ionization via a high-order Coulomb-corrected strong-field approximation, *Physical Review A* **95**, 023403 (2017).
- [34] M. Klaiber, K. Z. Hatsagortsyan, and C. H. Keitel, Relativistic analytical R-matrix theory for strong-field ionization, *Physical Review A* **107**, 023107 (2023).
- [35] L. V. Keldysh, Ionization in the field of a strong electromagnetic wave, *Sov. Phys. JETP* **20**, 1307 (1965).
- [36] F. H. Faisal, Multiple absorption of laser photons by atoms, *Journal of Physics B: Atomic and Molecular Physics* **6**, L89 (1973).
- [37] H. R. Reiss, Effect of an intense electromagnetic field on a weakly bound system, *Phys. Rev. A* **22**, 1786 (1980).
- [38] R. Santra, R. W. Dunford, and L. Young, Spin-orbit effect on strong-field ionization of krypton, *Physical Review A* **74**, 043403 (2006).
- [39] U. Fano, Spin Orientation of Photoelectrons Ejected by Circularly Polarized Light, *Physical Review* **178**, 131 (1969).
- [40] P. Lambropoulos, Spin-Orbit Coupling and Photoelectron Polarization in Multiphoton Ionization of Atoms, *Physical Review Letters* **30**, 413 (1973).
- [41] J. Kaushal and O. Smirnova, Looking inside the tunnelling barrier III: Spin polarisation in strong field ionisation from orbitals with high angular momentum, *Journal of Physics B: Atomic, Molecular and Optical Physics* **51**, 174003 (2018).
- [42] I. Barth and O. Smirnova, Nonadiabatic tunneling in circularly polarized laser fields: Physical picture and calculations, *Physical Review A - Atomic, Molecular, and Optical Physics* **84**, 063415 (2011).
- [43] T. Herath, L. Yan, S. K. Lee, and W. Li, Strong-Field Ionization Rate Depends on the Sign of the Magnetic Quantum Number, *Physical Review Letters* **109**, 043004 (2012).
- [44] S. Eckart, M. Kunitski, M. Richter, A. Hartung, J. Rist, F. Trinter, K. Fehre, N. Schlott, K. Henrichs, L. P. H. Schmidt, T. Jahnke, M. Schöffler, K. Liu, I. Barth, J. Kaushal, F. Morales, M. Ivanov, O. Smirnova, and R. Dörner, Ultrafast preparation and detection of ring currents in single atoms, *Nature Physics* **14**, 701 (2018).

- [45] D. Trabert, A. Hartung, S. Eckart, F. Trinter, A. Kalinin, M. Schöffler, L. P. H. Schmidt, T. Jahnke, M. Kunitski, and R. Dörner, Spin and Angular Momentum in Strong-Field Ionization, *Physical Review Letters* **120**, 43202 (2018).
- [46] D. Zille, D. Seipt, M. Möller, S. Fritzsche, S. Gräfe, C. Müller, and G. G. Paulus, Spin-dependent rescattering in strong-field ionization of helium, *Journal of Physics B: Atomic, Molecular and Optical Physics* **50**, 065001 (2017).
- [47] D. B. Milošević, Spin-dependent effects in high-order above-threshold ionization: Spin-orbit interaction and exchange effects, *Journal of Physics B: Atomic, Molecular and Optical Physics* **50**, 164003 (2017).
- [48] I. Barth and O. Smirnova, Hole dynamics and spin currents after ionization in strong circularly polarized laser fields, *Journal of Physics B: Atomic, Molecular and Optical Physics* **47**, 204020 (2014).
- [49] J. Kaushal, F. Morales, L. Torlina, M. Ivanov, and O. Smirnova, Spin-orbit Larmor clock for ionization times in one-photon and strong-field regimes, *Journal of Physics B: Atomic, Molecular and Optical Physics* **48**, 234002 (2015).
- [50] S. Carlström, J. M. Dahlström, M. Y. Ivanov, and S. Patchkovskii, Rydberg atomic antenna in strongly driven multielectron atoms, *Physical Review A* **106**, 043114 (2022).
- [51] S. Zhong, J. Vinbladh, D. Busto, R. J. Squibb, M. Isinger, L. Neorić, H. Laurell, R. Weissenbilder, C. L. Arnold, R. Feifel, J. M. Dahlström, G. Wendin, M. Gisselbrecht, E. Lindroth, and A. L’Huillier, Attosecond electron-spin dynamics in Xe 4d photoionization, *Nature Communications* **11**, 5042 (2020).
- [52] S. Carlström, J. M. Dahlström, M. Y. Ivanov, O. Smirnova, and S. Patchkovskii, *Control of Spin Polarization through Recollisions* (2023), [arxiv:2306.12823](https://arxiv.org/abs/2306.12823) [physics].
- [53] X. Y. Lai, C. Poli, H. Schomerus, and C. Figueira De Morisson Faria, Influence of the Coulomb potential on above-threshold ionization: A quantum-orbit analysis beyond the strong-field approximation, *Phys. Rev. A* **92**, 043407 (2015).
- [54] X. Lai, S. Yu, Y. Huang, L. Hua, C. Gong, W. Quan, C. F. d. M. Faria, and X. Liu, Near-threshold photoelectron holography beyond the strong-field approximation, *Physical Review A* **96**, 013414 (2017).
- [55] A. S. Maxwell, A. Al-Jawahiry, T. Das, and C. Figueira De Morisson Faria, Coulomb-corrected quantum interference in above-threshold ionization: Working towards multi-trajectory electron holography, *Phys. Rev. A* **96**, 023420 (2017).
- [56] A. S. Maxwell, A. Al-Jawahiry, X. Y. Lai, and C. F. d. M. Faria, Analytic quantum-interference conditions in Coulomb corrected photoelectron holography, *Journal of Physics B: Atomic, Molecular and Optical Physics* **51**, 044004 (2018).
- [57] A. S. Maxwell and C. F. d. M. Faria, Coulomb-free and Coulomb-distorted recolliding quantum orbits in photoelectron holography, *Journal of Physics B: Atomic, Molecular and Optical Physics* **51**, 124001 (2018).
- [58] A. S. Maxwell, S. V. Popruzhenko, and C. F. D. M. Faria, Treating branch cuts in quantum trajectory models for photoelectron holography, *Physical Review A* **98**, 1 (2018).
- [59] W. Becker, F. Grasbon, R. Kopold, D. B. Milošević, G. G. Paulus, and H. Walther, Above-Threshold Ionization: From Classical Features to Quantum Effects, in *Advances In Atomic, Molecular, and Optical Physics*, Vol. 48, edited by B. Bederson and H. Walther (Academic Press, 2002) pp. 35–98.
- [60] D. B. Milošević, G. G. Paulus, D. Bauer, and W. Becker, Above-threshold ionization by few-cycle pulses, *Journal of Physics B: Atomic, Molecular and Optical Physics* **39**, R203 (2006).
- [61] K. Amini, J. Biegert, F. Calegari, A. Chacón, M. F. Ciappina, A. Dauphin, D. K. Efimov, C. Figueira de Morisson Faria, K. Giergiel, P. Gniewek, A. S. Landsman, M. Lesiuk, M. Mandrysz, A. S. Maxwell, R. Moszyński, L. Ortmann, J. A. Pérez-Hernández, A. Picón, E. Pisanty, J. Prauzner-Bechcicki, K. Sacha, N. Suárez, A. Zaïr, J. Zakrzewski, and M. Lewenstein, Symphony on strong field approximation, *Reports on Progress in Physics* **82**, 116001 (2019).
- [62] H. Kang, A. S. Maxwell, D. Trabert, X. Lai, S. Eckart, M. Kunitski, M. Schöffler, T. Jahnke, X. Bian, R. Dörner, and C. F. D. M. Faria, Holographic detection of parity in atomic and molecular orbitals, *Physical Review A* **102**, 013109 (2020).
- [63] A. S. Maxwell, C. F. D. M. Faria, X. Y. Lai, R. P. Sun, and X. J. Liu, Spiral-like holographic structures: Unwinding interference carpets of Coulomb-distorted orbits in strong-field ionization, *Physical Review A* **102**, 033111 (2020).
- [64] N. Werby, A. S. Maxwell, R. Forbes, P. H. Bucksbaum, and C. F. d. M. Faria, Dissecting subcycle interference in photoelectron holography, *Physical Review A* **104**, 013109 (2021).
- [65] N. Werby, A. S. Maxwell, R. Forbes, C. F. d. M. Faria, and P. H. Bucksbaum, Probing two-path electron quantum interference in strong-field ionization with time-correlation filtering, *Physical Review A* **106**, 033118 (2022).
- [66] S. Brennecke, N. Eicke, and M. Lein, Gouy’s Phase Anomaly in Electron Waves Produced by Strong-Field Ionization, *Physical Review Letters* **124**, 153202 (2020).
- [67] L. C. Rodriguez, T. Rook, B. B. Augstein, A. S. Maxwell, and C. F. d. M. Faria, *Forward and hybrid path-integral methods in photoelectron holography: Sub-barrier corrections, initial sampling and momentum mapping* (2023), [arxiv:2305.14501](https://arxiv.org/abs/2305.14501) [physics, physics:quant-ph].
- [68] M. B. Carlsen, E. Hansen, L. B. Madsen, and A. S. Maxwell, A precise path-integral model with advanced momentum sampling and Maslov phases for strong-field ionization (2023), [Preprint:Preprint](https://arxiv.org/abs/2305.14501).
- [69] Technically $H[\mathbf{r}, \mathbf{p}, t']$ is the Weyl transformed quantum-mechanical Hamiltonian [107], which differs from the classical Hamiltonian $H[\mathbf{p}, \mathbf{r}, t'] = K[\mathbf{p}] + U[\mathbf{r}] + H_I(t')$ by orders of \hbar^2 , however these differences may be discarded given we will be applying the saddle-point approximation that already neglects the quadratic power of \hbar .
- [70] N. I. Shvetsov-Shilovski, Semiclassical two-step model for ionization by a strong laser pulse: Further developments and applications, *The European Physical Journal D* **75**, 130 (2021).
- [71] T.-M. Yan, S. V. Popruzhenko, M. J. J. Vrakking, and D. Bauer, Low-Energy Structures in Strong Field Ion-

- ization Revealed by Quantum Orbits, *Phys. Rev. Lett.* **105**, 253002 (2010).
- [72] V. Tulsy and D. Bauer, QPROP with faster calculation of photoelectron spectra, *Computer Physics Communications* **251**, 107098 (2019).
- [73] C. Figueira de Morisson Faria, H. Schomerus, and W. Becker, High-order above-threshold ionization: The uniform approximation and the effect of the binding potential, *Physical Review A* **66**, 043413 (2002).
- [74] L. Kocia and A. Klales, Semiclassical treatment of quantum propagation with nonlinear classical dynamics: A third-order thawed Gaussian approximation, *Physical Review E* **94**, 032211 (2016).
- [75] P. Strange, *Relativistic Quantum Mechanics: With Applications in Condensed Matter and Atomic Physics*, 1st ed. (Cambridge University Press, Cambridge, 1998).
- [76] H. R. Reiss, Limits on Tunneling Theories of Strong-Field Ionization, *Physical Review Letters* **101**, 043002 (2008).
- [77] J. R. Klauder, Path integrals and stationary-phase approximations, *Physical Review D* **19**, 2349 (1979).
- [78] M. Pletyukhov, Ch. Amann, M. Mehta, and M. Brack, Semiclassical Theory of Spin-Orbit Interactions using Spin Coherent States, *Physical Review Letters* **89**, 116601 (2002).
- [79] B. H. Bransden and C. J. Joachain, *Physics of Atoms and Molecules* (Longman Scientific & Technical, Burnt mill, Harlow, 1983).
- [80] E. A. Kochetov, SU(2) coherent-state path integral, *Journal of Mathematical Physics* **36**, 4667 (1995).
- [81] M. Pletyukhov and O. Zaitsev, Semiclassical theory of spin orbit interaction in the extended phase space, *Journal of Physics A: Mathematical and General* **36**, 5181 (2003).
- [82] K. Morten, *A Path Integral Approach to The Spin-Orbit Interaction*, Ph.D. thesis, Nano-Science Center, Copenhagen University (2008).
- [83] T. J. Lemmon and A. R. Mondragon, *Kepler's Orbits and Special Relativity in Introductory Classical Mechanics* (2016), [arxiv:1012.5438](https://arxiv.org/abs/1012.5438) [astro-ph, physics:physics].
- [84] This is because, in the weak-coupling limit, the effect of spin-orbit coupling on the electronic motion is neglected.
- [85] C. I. Blaga, J. Xu, A. D. DiChiara, E. Sistrunk, K. Zhang, P. Agostini, T. A. Miller, L. F. DiMauro, and C. D. Lin, Imaging ultrafast molecular dynamics with laser-induced electron diffraction, *Nature* **483**, 194 (2012).
- [86] B. Wolter, M. G. Pullen, A.-T. Le, M. Baudisch, K. Doblhoff-Dier, A. Senftleben, M. Hemmer, C. D. Schröter, J. Ullrich, T. Pfeifer, R. Moshhammer, S. Gräfe, O. Vendrell, C. D. Lin, and J. Biegert, Ultrafast electron diffraction imaging of bond breaking in di-ionized acetylene, *Science* **354**, 308 (2016).
- [87] A. Gorlach, O. Neufeld, N. Rivera, O. Cohen, and I. Kaminer, The quantum-optical nature of high harmonic generation, *Nature Communications* **11**, 4598 (2020).
- [88] M. Lewenstein, M. F. Ciappina, E. Pisanty, J. Rivera-Dean, P. Stammer, T. Lamprou, and P. Tzallas, Generation of optical Schrödinger cat states in intense laser-matter interactions, *Nature Physics* **17**, 1104 (2021).
- [89] P. Stammer, J. Rivera-Dean, T. Lamprou, E. Pisanty, M. F. Ciappina, P. Tzallas, and M. Lewenstein, High Photon Number Entangled States and Coherent State Superposition from the Extreme Ultraviolet to the Far Infrared, *Physical Review Letters* **128**, 123603 (2022).
- [90] J. Rivera-Dean, P. Stammer, A. S. Maxwell, Th. Lamprou, P. Tzallas, M. Lewenstein, and M. F. Ciappina, Light-matter entanglement after above-threshold ionization processes in atoms, *Physical Review A* **106**, 063705 (2022).
- [91] P. Stammer, J. Rivera-Dean, A. Maxwell, T. Lamprou, A. Ordóñez, M. F. Ciappina, P. Tzallas, and M. Lewenstein, Quantum Electrodynamics of Intense Laser-Matter Interactions: A Tool for Quantum State Engineering, *PRX Quantum* **4**, 010201 (2023).
- [92] A. Pizzi, A. Gorlach, N. Rivera, A. Nunnenkamp, and I. Kaminer, Light emission from strongly driven many-body systems, *Nature Physics* **19**, 551 (2023).
- [93] M. Even Tzur, M. Birk, A. Gorlach, M. Krüger, I. Kaminer, and O. Cohen, Photon-statistics force in ultrafast electron dynamics, *Nature Photonics* **17**, 501 (2023).
- [94] A. S. Maxwell, G. S. J. Armstrong, M. Ciappina, E. Pisanty, Y. Kang, A. Brown, M. Lewenstein, and C. Figueira de Morisson Faria, Manipulating Twisted Electrons in Strong Field Ionization, *Faraday Discussions*, 394 (2020).
- [95] Y. Kang, E. Pisanty, M. Ciappina, M. Lewenstein, C. Figueira de Morisson Faria, and A. S. Maxwell, Conservation laws for electron vortices in strong-field ionisation, *The European Physical Journal D* **75**, 199 (2021).
- [96] X. B. Planas, A. Ordóñez, M. Lewenstein, and A. S. Maxwell, Ultrafast Imaging of Molecular Chirality with Photoelectron Vortices, *Physical Review Letters* **129**, 233201 (2022).
- [97] A. S. Maxwell, L. B. Madsen, and M. Lewenstein, Entanglement of orbital angular momentum in non-sequential double ionization, *Nature Communications* **13**, 4706 (2022).
- [98] S. V. B. Jensen, M. M. Lund, and L. B. Madsen, Nondipole strong-field-approximation Hamiltonian, *Physical Review A* **101**, 043408 (2020).
- [99] L. B. Madsen, Nondipole effects in tunneling ionization by intense laser pulses, *Physical Review A* **105**, 043107 (2022).
- [100] S. Brennecke and M. Lein, High-order above-threshold ionization beyond the electric dipole approximation: Dependence on the atomic and molecular structure, *Physical Review A* **98**, 063414 (2018).
- [101] L. B. Madsen, Disappearance and reappearance of above-threshold-ionization peaks, *Physical Review A* **106**, 043118 (2022).
- [102] B. Wolter, M. G. Pullen, M. Baudisch, M. Sclafani, M. Hemmer, A. Senftleben, C. D. Schröter, J. Ullrich, R. Moshhammer, and J. Biegert, Strong-field physics with Mid-IR fields, *Phys. Rev. X* **5**, 021034 (2015).
- [103] N. I. Shvetsov-Shilovski, M. Lein, L. B. Madsen, E. Räsänen, C. Lemell, J. Burgdörfer, D. G. Arbó, and K. Tórkési, Semiclassical two-step model for strong-field ionization, *Phys. Rev. A* **94**, 013415 (2016), [arxiv:1604.05123](https://arxiv.org/abs/1604.05123).
- [104] A. M. Perelomov, V. S. Popov, and M. Terent'ev, Ionization of atoms in an alternating electrical field, *Sov. Phys. JETP* **23**, 924 (1966).

- [105] C. Z. Bisgaard and L. B. Madsen, Tunneling ionization of atoms, *American Journal of Physics* **72**, 249 (2004).
- [106] W. A. Adkins and M. G. Davidson, Linear Systems of Differential Equations, in *Ordinary Differential Equations*, Undergraduate Texts in Mathematics, edited by W. A. Adkins and M. G. Davidson (Springer, New York, NY, 2012) pp. 629–721.
- [107] M. M. Mizrahi, The Weyl correspondence and path integrals, *Journal of Mathematical Physics* **16**, 2201 (1975).